RAMAN – MICROSCOPY OF INDIVIDUAL CELLS

AND

APPLICATIONS MONITORING DRUG UPTAKE

by

CHRISTIAN B. MATTHAEUS

A dissertation submitted to the Graduate Faculty in Chemistry in partial fulfillment of the requirements for the degree of Doctor of Philosophy, The City University of New York

2006

UMI Number: 3205013

ProQuest Information and Learning Company
300 North Zeeb Road
P.O. Box 1346
Ann Arbor, MI 48106-1346

This manuscript has been read and accepted for the
Graduate Faculty in Chemistry in satisfaction of the
dissertation requirement for the degree of Doctor of Philosophy.

Max Diem

Date — Chair of Examining Committee

Gerald Koeppl

Date — Executive Officer

Dr. Luis Chiriboga

Prof. C. Michael Drain

Prof. Richard Mendelsohn

Prof. Thomas Strekas
Supervision Committee

THE CITY UNIVERSITY OF NEW YORK

Abstract

RAMAN – MICROSCOPY OF INDIVIDUAL CELLS

AND

APPLICATIONS MONITORING DRUG UPTAKE

by

Christian Matthaeus

Adviser: Professor Max Diem

Raman imaging of individual cells has become a quite useful technique providing spectral information at very reasonable signal quality. Based on the spectral parameters of a cell's components it is possible to image subcellular compartments such as nucleus or nucleoli at micrometer spatial resolution. Apparent advantages over conventional staining procedures are the noninvasive character of the technique as well as the associated chemical information. Depending on the optical setup Raman microscopy can be employed after cell fixation or on living cells. One intriguing application of Raman microscopy is monitoring the uptake of cytotoxins that are for example used in chemotherapy. The spectral information allows imaging the subcellular distribution of the drug as well as speculation about its chemical faith based on spectral changes. In chapter 3, the capability of Raman microscopy to image subcellular compartments is demonstrated. First by univariate intensity imaging, followed by introducing spectral imaging based on multivaried statistical clustering analysis. Chapter 4 addresses the potential of the technique to study drug uptake in *in vitro* type cell cultures.

Acknowledgements

First, I would like to thank my mentor Professor Max Diem for the possibility to conduct the research in his group. He has supported me in every possible respect allowing a great amount of freedom to carry out various experiments. Second, I would like to thank my committee members, Dr. Luis Chiriboga, Professor Richard Mendelssohn, Professor Michael Drain and Professor Thomas Strekas, for guiding me trough all those years. Special thanks go to Professor Cees Otto and Henk-Jan van Manen from the University of Twente in the Netherlands for their help and collaboration, especially on the drug uptake experiments. I would like to thank Professor Lakshman for providing the benzopyrene derivatives. Furthermore, I would like to thank my colleagues in the laboratory, Miloš Miljković, Melissa Romeo, Susie Boydston-White, Brian Mohlenhoff, Tatjana Chernenko and Sebastian Thompson for very stimulating discussions. Above all, I thank my wife Marina for constant support throughout the years.

Table of Contents:

List of Figures:

Chapter 1: Introduction

The coupling of a Raman system to the optics of a microscope and thus, the possibility of simultaneous optical as well as spectroscopic inspection on a micrometer scale, offers a variety of applications. Recent publications of biological studies can be roughly divided into the areas of cell biology, tissue characterization and typing of microorganisms.

Raman microscopy has been used to observe metabolic activity of single living cells such as NADPH-oxidase activity inside granulocytes, important for the activation process of those cells,[1-3] lipid body accumulation around phagosomes in leucocytes[4] or hemoglobin oxidation and heme aggregation in erythrocytes.[5] The degeneration of proteins during necrosis may be monitored by changes in the appearance of Raman spectra.[6] There have been attempts to introduce Raman labels, i.e. molecules that have a high Raman scattering cross section, to detect cellular enzymes and receptors.[7]

In terms of cell imaging Raman microscopy has been employed to image subcellular features such as the nucleus[8] and mitochondria.[9] First results have been published to image the uptake of cytotoxins utilizing resonance and pre-resonance effects.[10, 11]

In general, differences in the texture and composition of any biological material may be discriminated by its spectroscopic features. Over the past ten years, several attempts have been made to establish Raman microscopy as an independent modality to distinguish between normal and diseased tissue. Usually, the grade and progression of tissue altering diseases, such as various tumor types and protein misfolding in the brain,

are determined by histo-pathological inspection based on conventional staining techniques. In several cases, it may be quite challenging to draw a line between normal and affected tissue.[12] Raman spectroscopy could provide an additional analytic tool that could help to quantify alterations in texture and composition of diseased tissue. Several studies demonstrating the capability of Raman spectroscopy to discriminate between normal and diseased tissue have been published. Interesting examples are the detection of meningioma in dura matter[12] and the detection of various cancer types such as ovarian cancer[13] or oral squamous cell carcinoma.[14] In some cases the spectral differences are too subtle to be distinguished by mere visual inspection. To aid the analytical process several unsupervised statistical evaluations have been developed which may be visualized by pseudo-color representations, providing additional information to the histo-pathology.[12] Spectral differences that have been classified by those statistical algorithms may subsequently serve as input data for artificial neural networks (ANNs).

Several studies have been performed to utilize Raman microscopy as an analytical implement to conventional typing methods to characterize microorganisms such as bacteria.[15-17] Again, statistical algorithms that have been established in the field have been proven to be reliable tools.

Chapter 2: Materials and methods

2.1. The Raman effect

If light hits a sample, the incoming electrical field sets the electrons of the molecules in motion, which induces a fluctuating dipole. Usually, the induced dipole emits electromagnetic vibrations of the same frequency. That (in a classical sense) elastic scattering is called Raleigh scattering. However, in the case that incoming photons excite molecular vibrations, the emitted photons will have less energy. That inelastic scattering event is called Raman scattering. Two scenarios are possible for the inelastic type of scattering. Either a photon hits a molecule in the ground state and excites molecular vibration or it hits a molecule already in the excited state and causes vibrational relaxation. In the first event, the scattered photons will be red shifted with respect to the Raleigh line in the second blue shifted. The lines are usually referred to as Stokes- and anti-Stokes-lines respectively. Figure 2.1.1. shows the energy diagrams for all three scattering events.

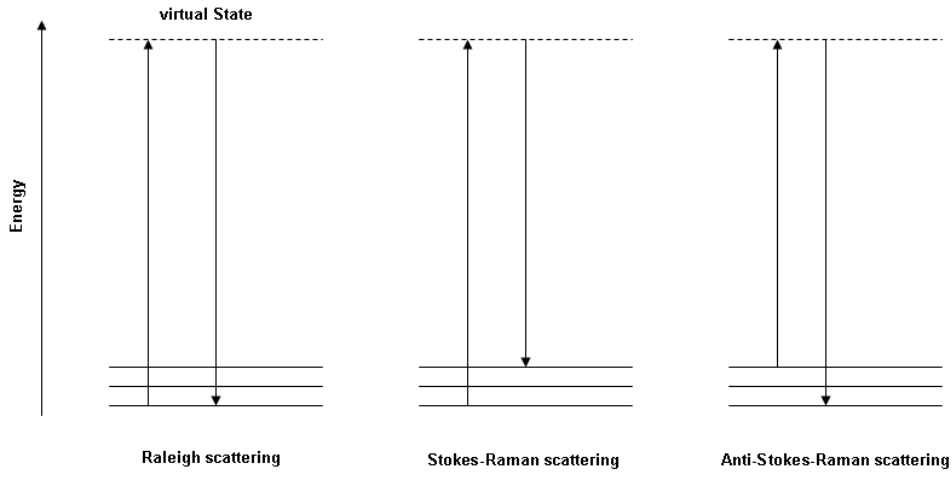

Figure 2.1.1.: Raman effect: schematic presentation of Raleigh-, Stokes-, and Anti-Stokes scattering

Scattering of radiation is a fast effect (roughly 10^{-14} sec) of interaction of a photon and a molecule and takes place when the photon energy does not correspond to the difference between any two stationary states of the molecule.

The intensity of the Raman scattering depends on the "flexibility" of the electron cloud of a particular molecule, which is described by its polarizability α. If E is the strength of the incoming electrical field, a dipole moment μ is induced:

$$\mu = \alpha E .$$

If E is the electrical field component of the exciting light with frequency ν_E one gets:

$$E = E_0 \cos 2\pi \nu_E t$$

$$\mu = \alpha E_0 \cos 2\pi \nu_E t ,$$

where t is the time. A molecule that vibrates with a frequency ν_i changes its normal coordinates according to:

$$q_i = Q_i \cos 2\pi \nu_i t ,$$

with q_i and Q_i representing the molecular vibrational coordinates and the normal coordinates at equilibrium position respectively. Changing the shape of a molecule, changes its polarizability to:

$$\alpha = \alpha_0 + \frac{\partial \alpha}{\partial q_i} q_i ,$$

where α_0 is the polarizability at the equilibrium position. Substitution into the second expression for the dipole moment (and introducing the trigonometric relation $2\cos x \cos y = \cos(x-y) + \cos(x+y)$ results in:

$$\mu = \alpha_0 E_0 \cos 2\pi \nu_E t + \frac{E_0 Q_i}{2} \frac{\partial \alpha}{\partial q_i} [\cos 2\pi(\nu_E - \nu_i)t + \cos 2\pi(\nu_E + \nu_i)t] .$$

According to this equation, the dipole moment μ oscillates with three superimposed frequencies ν_E, $\nu_E - \nu_i$ and $\nu_E + \nu_i$, corresponding to Raleigh scattering, Stokes-, and anti-Stokes-Raman scattering.[18, 19]

If the excitation frequency of the exciting light beam is of the same energy as an electronic transition, the molecule is excited into a stationary electronic state. The emision of a photon may also result in a vibrationally excited state. The phenomenon is of the same nature as described in Figure 2.1.1., with the difference that the emitted photon does not result from a virtual state but from a well defined electronic state. Light scattering in resonance with an electronic transition causes an enhancement up to four orders of magnitude in intensity compared with the conventional Raman effect. The intensity enhancement of a particular Raman band is related to the nature of the vibration and structural vibrations that are involved in the electronic transition. The dependence of the intensities of resonance Raman bands may be described by:

$$I \propto \left[\frac{(\nu_E - \nu_i)^2 (\nu_A^2 + \nu_E^2)}{(\nu_A^2 - \nu_E^2)^2} \right]^2,$$

where ν_A is the electron excitation frequency, ν_E the frequency of the exciting light beam and ν_i the vibrational frequency. If $\nu_A = \nu_E$ resonance Raman scattering, and if $\nu_A << \nu_E$, $\nu_A >> \nu_E$ conventional Raman scattering is observed. Enhancement effects observed for $\nu_A \approx \nu_E$ are referred to as pre-resonance Raman effects. Usually, more than one excitation have to be taken into account which makes the interpretation of the enhancement of individual Raman bands complicated.[18]

2.2. Experimental setup

To obtain Raman signals from microscopic samples, the exciting laser beam is coupled to a general microscope. A simplified setup is shown in Figure 2.1. The laser beam first hits a half-dichroic mirror or beam splitter (BS). The reflected light is then focused on the sample through an objective. The scattered light that again passes the objective hits a notch filter (NF) that reduces the Raleigh intensity. Lens L2 focuses the beam through a confocal pinhole (PH) before it enters a spectrograph or monochromator and finally the detector. For imaging, the microscope can be coupled to an automated x,y,z-stage. Alternatively, a scanning mirror can be placed in front of the focusing lens L1. To switch between observation and measurement usually a swinging-mirror is also placed in the beam line.

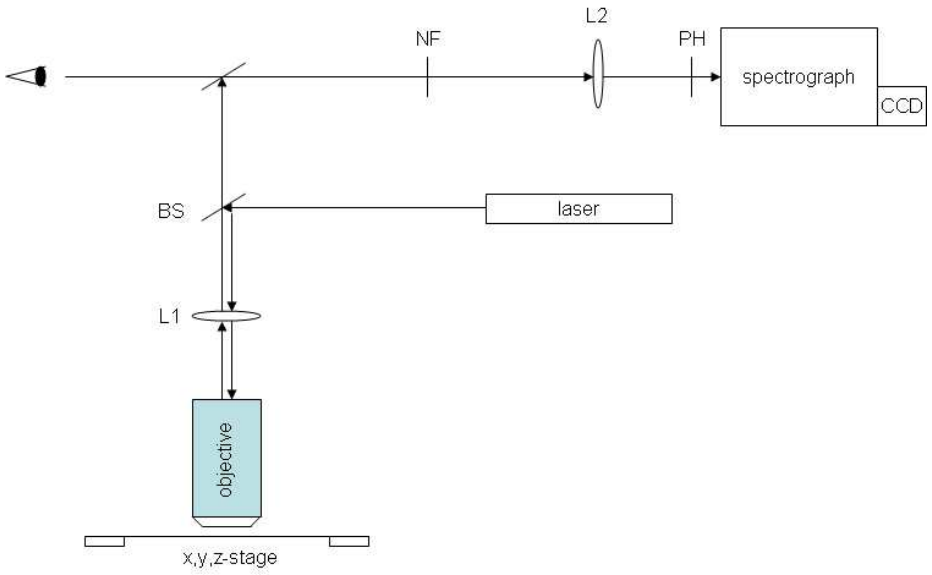

Figure 2.2.1.: Optical setup for Raman microscopes: NF = notch filter, BS = beam splitter, L1,2 = focusing lenses, PH = pin hole

Since most laser wavelengths applied in the field are in the visible spectrum of light, the critical optical parameters are similar to those for conventional microscopy. The spatial resolution along the image field, perpendicular to the optical axis is given by:

$$d = 1.22\frac{\lambda_0}{2NA_{obj}},$$

where d is the minimum distance of two point objects just resolved by the microscope, λ_0 is the wavelength of the incident light beam and NA the numerical aperture of the objective.[20] For a 632.8nm HeNe laser and a numerical aperture of 0.9 for the objective, the limiting resolution would then be 429nm. The in depth resolution (DR) along the optical axis is determined by:

$$DR = 2.2\frac{n\lambda}{\pi\left(NA_{obj}\right)^2},$$

where n is the refractive index of the immersion medium, λ again the wavelength of the incident light beam and NA the numerical aperture.[21] For a 632.8nm excitation the theoretical limiting resolution is 547nm. In general, no resolution along the optical axis can be obtained because light is not only collected from the focal plane of the sample, but also from adjacent layers. Light diffusion and scattering on uneven surfaces further complicate this situation. In order to improve the in depth resolution Raman microscopes are usually equipped with a confocal arrangement. In confocal fluorescence microscopy the setup allows sequencing a sample along the optical axis and hence 3D imaging. Raman microscopy is very similar in this respect because unlike in optical microscopy the incoming light and thus the resolution are very well defined. In confocal microscopy a pinhole is placed at the back focal plane of the microscope. The pinhole is conjugate to the focal point of the lens. As shown in Figure 2.2. only light that is generated at focal

point A passes the pinhole, whereas light that originates from B or C is blocked by the aperture.

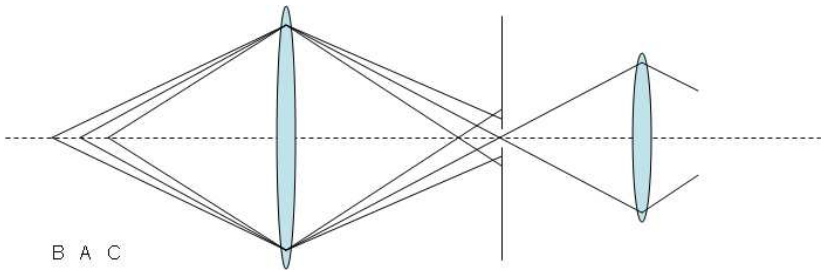

Figure 2.2.2.: Confocal optics, only light generated at focal point A passes the pinhole

All experiments presented in this study were carried out on the LabRam HR800 microscope by Jobin-Yvon Horiba. The system is equipped with a 632.8nm HeNe-laser that has a power output of 20mW. An air-cooled CCD camera with 1024x256 pixels of 26µm serves as detector. The spectrograph is a 800mm focal length Czerny Turner spectrograph with a 1800g/mm grating, which allows a spectral resolution of $1cm^{-1}$. The coupled microscope is a high stability BX40 Olympus microscope with 10x (NA=0.25), 50x (NA=0.7), and 100x (NA=0.9) objectives.

2.3. Data Treatment

2.3.1. Smoothing Procedures

Main sources of noise in Raman spectroscopy originate from dark current of the detector, inelastic scattering from particles (Tyndall scattering) as well as flicker noise

from the source.[22] In the case of low signal quality, mathematical procedures to reduce the given noise level may be useful if not essential.

One simple way of reducing random noise is by a moving average. Given a set of data points X_n with assigned readouts C_n the procedure averages a chosen number of neighboring data points C_{n+2}, C_{n+1}, C_{n-1}, C_{n-2} and replaces the center point C_0 with the mean average. C_0 is called a single convolute and C_{n+2},…, C_{n-2} are convoluting integers. For the next point the set of convoluting integers are moved to the next data point and the procedure is repeated. In the end a new function X_n is obtained:

$$X_j^* = \frac{\sum_{i=-n}^{i=n} C_i X_{j+i}}{2n+1}.$$

The set of convoluting integers C_i is referred to as convolution function. In the case of a moving average, all neighboring data points over the chosen interval are assigned the same weight. Other convolution functions introduce a steady or exponential decay for the weight of adjacent data points as illustrated in Figure 2.3.1.

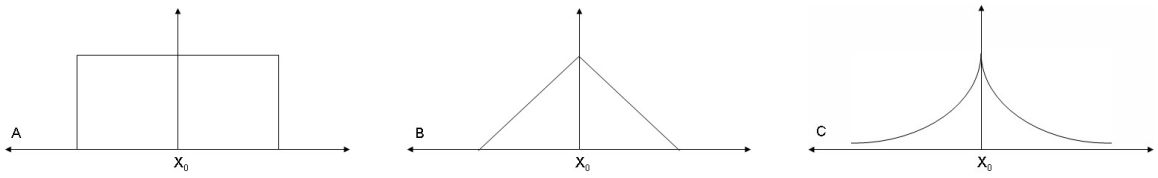

Figure 2.3.1.: Convolution functions for a moving average (A), a steady decay (B), and an exponential decay (C)

Savitzky and Golay suggested using polynomials such as $y = a_0 + a_1 x + a_2 x^2 + ...a_k{}^k$ as convolution functions and fit them with partial least squares.[23] The fitting method first defines a residual data point r_i as a distance between an observed data point y_i and a fitted response value $\hat{y}_i$:

$$r_i = y_i - \hat{y}_i .$$

The residual data points are expressed as standard deviations:

$$R^2 = \sum_{i=1}^{n} r_i^2 = \sum_{i=1}^{n} (y_i - \hat{y}_i)^2 .$$

For a nonlinear fit R^2 is expressed as:

$$R^2 = \sum_{i=1}^{n} [y_i - (a_0 + a_1 x_i + a_2 x_i{}^2 + ... + a_k x_i{}^k)]^2 .$$

To minimize the deviation, all partial derivatives with respect to the a_k's have to be zero:

$$\frac{\partial(R^2)}{\partial a_k} = 0 ,$$

$$\frac{\partial(R^2)}{a_0} = -2\sum_{i=1}^{n} [y_i - (a_0 + a_1 x_i + ... + a_k x_i^k)] = 0 ,$$

$$\frac{\partial(R^2)}{a_1} = -2\sum_{i=1}^{n} [y_i - (a_0 + a_1 x_i + ... + a_k x_i^k)] x_i = 0 ,$$

$$\frac{\partial(R^2)}{a_k} = -2\sum_{i=1}^{n} [y_i - (a_0 + a_1 x_i + ... + a_k x_i^k)] x_i{}^k = 0 .$$

After evaluating the values for the a's one substitutes for the central data point and precedes picking up the next data point on the right, while dropping one on the left and so forth.

2.3.2. Cluster Analysis

Any vibrational spectrum provides qualitative and quantitative chemical information about the composition of the sample of interest. The chemical information is represented by characteristic peaks as well as by their individual band shapes. For a quantitative analysis, especially for large datasets a number of statistical procedures, based on a comparison of the similarity of the individual spectra have been developed. Relatively well established for data analysis of vibrational spectra are procedures such as principal component analysis (PCA), fuzzy c-means clustering or hierarchical clustering.[13, 24] All methods search for spectral differences that are not obvious by mere visual inspection. For imaging of biological samples especially the hierarchical clustering procedure has been proven to be very useful. One main application has been infrared and Raman spectroscopic imaging of diseased tissue such as tissue from cancer and various other illnesses.[25]

In hierarchical cluster analysis (HCA) the similarity of the spectra is expressed as a matrix of correlation coefficients C_{LM}:

$$C_{LM} = \frac{\sum_{i=1}^{N}(S_i^L - \overline{S^L})(S_i^M - \overline{S^M})}{\sqrt{\sum_{i}^{N}(S_i^L - \overline{S^L})^2}\sqrt{\sum_{i}^{N}(S_i^M - \overline{S^M})^2}},$$

where S^L and S^M are two individual spectra of the dataset. The correlation matrix C_{LM} contains N^2 entries, where N is the total number of spectra. The Correlation coefficients can be also seen as normalized vector dot products ranging from zero to one, with $C_{LM} = 1$ for identical spectra and $C_{LM} = 0$ for spectra with no overlap.

Mathematical algorithms then search for the closest C_{LM} terms and merge two corresponding spectra into a new object. The correlation matrix is recalculated and the merging process repeated until all spectra have been combined into a small number of clusters.

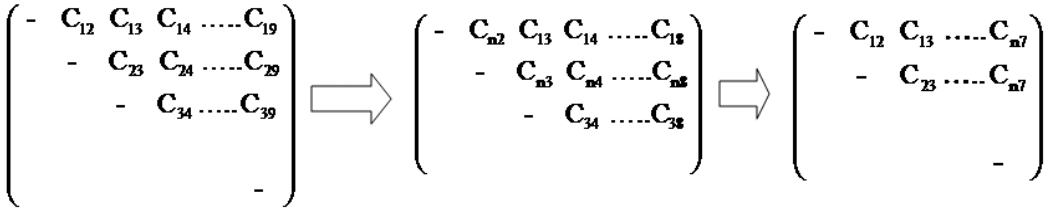

Each cluster can be assigned a color and displaying the individual colors at the coordinates at which the spectra where collected creates a pseudo-color map based on the spectral information. The maps also known as false-color images represent the similarity of the chemical composition of the substrate.

2.3.3. Vector Normalization

In order to detect or image spectral differences independent of the sample thickness it is in some cases necessary to scale or normalize the collected spectra. Especially for the above mentioned HCA routine, the normalization of the datasets is essential. The vector normalization was carried out by first calculating the average value for the indicated spectral region. The average value was then subtracted from the particular spectrum setting the new average to zero. Subsequently, the sum over all data points of the spectrum was scaled to one:

$$\sum_i (x_i)^2 = 1.$$

2.4. Cell cultures

Mammalian cells can be cultured in an *in vitro* environment under temperature and pH controlled growth conditions. Cellular metabolism is maintained by essential growth factors dissolved in the culture medium. Cell cultures may be initiated from normal, embryonic and malignant tissues or cells. Generally, there are two categories: Cells, which grow in suspension, and cells that adhere to substances such as glass or plastic by mucoproteins and in some cases collagen. Adherent cells are usually described as fibroblast-like or epithelial-like. Fibroblasts are connective tissue cells. In dilute culture, they move around the surface of the substrate avoiding each other. Epithelial cells origin from the surface of an organ such as the cervix or kidney tubules. The cells are tightly associated and divide to form sheets of cells. Somatic cells that adhere to a certain substrate grow exponentially in monolayers until they reach confluence. Attachment to the substrate is usually vital, and cells that form a second layer normally die. Once confluence is reached, the cells have to be subcultured, i.e. split over more than one culture vessel. Non-adherent cells such as leucocytes require subculturing when the medium rapidly turns acidic after feeding. Such cell cultures are referred to as cell lines, whereas cultures initiated from tissue are called primary cultures. Cell lines from embryonic cells normally live through some 50 generations. Adult cells may be maintained for 20 generations.

During the early stages the cells remain euploid, i.e. they have the correct diploid complement of chromosomes. Associated with the cells aging process are mutations in

the DNA, which may result in packing disorders and abnormal gene expressions. If those transformed cells survive, the cell culture may become “immortal”. Transformation may also occur *in vivo*. Many cell lines that were originally derived from tumor tissues grow indefinitely *in vitro*. Transformed cells loose their density dependent regulation properties and, in contrast to untransformed cells, grow until the medium is exhausted.

The growth medium usually contains some 30 essential factors such as amino acids, vitamins and glucose. Eagle originally developed the optimal composition for a variety of cells in the 1950’s. Most cell lines also rely on natural serum extracts, which contain adhesion promoting components, trace minerals, transport proteins, growth factors and hormones. Bovine or fetal calf serum is normally added in amounts of 5% to 10%.

For subculturing, digesting enzymes such as trypsin may be added to the medium. It reduces the amount of mucoproteins, which link the cells with the substrate. In addition, complexing agents such as EDTA are often used to remove divalent cations particularly Ca^{2+} and Mg^{2+}, which play a role in intracellular binding.

2.4.1. Adherent cells

Human epithelial cells from the HeLa CCL-2 cell line were obtained from ATCC (American Type Culture Collection (ATCC), Manassas, VA). The cell line originates from a cervical adenocarcinoma. Cells were grown in Minimum Essential Medium (Eagle) with 2 mM L-glutamine and Earle's BSS adjusted to contain 1.5 g/L sodium bicarbonate, 0.1 mM non-essential amino acids, and 1.0 mM sodium pyruvate, 90%; fetal

bovine serum, 10%, and incubated at 37ºC in an atmosphere of 95% air with 5% CO_2. Subculturing was performed according to the following protocol.

1. Removal of the culture medium.
2. The cell container was rinsed with phosphate buffered saline (PBS) solution.
3. For a 30ml flask, 2ml of a 0.25% (w/v) Trypsin- 0.53 mM EDTA solution were added and incubated for 5min until all cells were detached from the surface of the flask.
4. 6ml to 8ml of medium were added. To avoid clumping the suspension was repeatedly pipeted.
5. The suspended cells were centrifuged for 5min at 3000rpm.
6. After removal of the suspension medium the cells were vortexed and subcultured with 6ml to 8ml fresh medium at splitting ratios of 1:2 to 1:5.
7. The growth medium was renewed every 2 to 3 days.

2.4.2. Non-adherent cells

Human T-lymphocytes from the Jurkat TIB-152 cell line, originating from acute T-cell leukemia were obtained from ATCC. Cells were grown in RPMI 1640 medium with 2 mM L-glutamine adjusted to contain 1.5 g/L sodium bicarbonate, 4.5 g/L glucose, 10 mM HEPES, and 1.0 mM sodium pyruvate, 90%; fetal bovine serum, 10%, and incubated at 37ºC in an atmosphere of 95% air with 5% CO_2. The cells were subcultured according to the following protocol.

1. The cell suspension was centrifuged for 5min at 1500rpm.

2. The exhausted medium was removed, the cells resuspended and subcultured at splitting ratios 1:2 to 1:5.
3. 6ml to 8ml of fresh growth medium were added to 30ml culture-flasks.
4. The growth medium was replaced every 2 to 3 days.

2.5. Sample preparation and cell fixation

Adherent cells were grown onto CaF_2 windows to avoid any background scattering from the surface of usual glass slides. The cell density was kept at a low level with roughly 10-20/mm^2 to allow mapping of individual cells and sustain large areas of cytoplasm. Cells were fixed in 10% phosphate buffered formalin solution for 10min to 20min at room temperature, subsequently briefly washed with distilled water and quick-dried under a compressed air stream. Aldehydes fix biological material by introducing cross-links between different cellular components such as protein, nucleic acids and lipids. The degree of cross-linking is proportional to the fixation time. Bonding is generated between several reactive groups, i.e. thiol- or amino-groups of cystein and lysine residues. Cross-linking fixation methods with formalin solutions or paraformaldehyde were found to give best microscopic and spectroscopic results. Alternative fixation methods in various organic compounds such as methanol, ethanol and acetone or freeze drying methods dehydrate the cells largely. Thus, shape and particularly cell thickness are not always preserved.

Lymphocytes were grown up to a concentration between 10^5/ml and $5x10^5$/ml. 0.5ml of cell suspension were added to 1ml of 10% phosphate buffered formalin solution.

After fixation the cells were spun onto CaF_2 windows using a Cytospin centrifuge for 15min at 400rpm with low acceleration.

2.6. Fluorescence Staining

Fluorescence microscopy is widely used to image cellular constituents. Although often difficult to reproduce, especially for site-specific staining with fluorescent antibodies, a variety of protocols is available. Usually the staining procedures employ surfactant solutions to increase the permeability of the cell membranes. In this study fluorescence staining was mainly used for chromatin imaging employing 4'-6-diamidino-2-phenylindole (DAPI) applying the following procedure.

1. Cells were rehydrated in PBS solution for 30min at room temperature.
2. Permeabilizing buffer, with 0.2% Triton X-100 in PBS, was added for 5min.
3. Cells were incubated in PBS with 0.02% Tween 20, 0.04% sodium azide (PBST) and subsequently treated with DAPI solution for 2min to 5min.
4. After washing three times with PBST, the slides were dipped into distilled water and quick-dried under a compressed air stream.

All images were acquired on a Nikon EFD-3 microscope using a Texas Red emission filter.

Chapter 3: Imaging of cellular compartments

3.1. Introduction

The distinct biochemical composition of cellular compartments, such as the nucleus, nucleoli or cytoplasm allows a classification based on their spectral features. The limiting spatial resolution is defined by the diffraction limit of the applied laser beam. Whatever the chemical composition within the scattering volume will be reflected in the associated spectra. The aim of this chapter is to discuss the extent that Raman microscopy can be used to image subcellular structures. First, results for normal cells grown *in vitro* are presented. The Raman spectra of the main cellular features are discussed in detail and Raman imaging based on single wavelength intensities is introduced. The plotting of spatially resolved univariate intensities will be referred to as spectral imaging. To illustrate the potential of spectral imaging, the technique was applied to monitor the chromatin distribution during mitosis. The second part of the chapter will address the possibility to image cellular features based on a comparison of band shape similarities, employing hierarchical clustering methods.

As cell model, human epithelial cells from the HeLa CCL-2 cell line were chosen. The cell line derives from a cervical carcinoma, which can be easily subcultured. The cells have adherent growth properties and vary in size from approximately 30µm to 100µm in diameter.

3.2. Spectral imaging

3.2.1. Results

Figure 3.2.3. shows HeLa cells grown onto a CaF_2 substrate. Easy to recognize are the nuclei, approximately 25µm in size, with distinct nucleoli inside. Figure 3.2.1. shows a typical Raman spectrum from the cytoplasm. In 3.2.1.a the whole spectral range from 4000cm^{-1} to 500cm^{-1} is plotted, whereas in 3.2.1.b the most characteristic region between 1800cm^{-1} and 500cm^{-1} is enlarged. The Raman spectra of biological molecules have been described in great detail.[26] For the random variety of proteins inside the cytoplasm only the main spectral features can be attributed. Most pronounced are the C – H stretching vibrations ranging from 3095cm^{-1} to 2800cm^{-1} with a center around 2934cm^{-1}. Also very pronounced are the C=O stretching vibrations of the peptide linkages between 1600cm^{-1} and 1700cm^{-1}. The band, usually referred to as amide I, is centered at 1655cm^{-1} with little variation. The small shoulder between 1530cm^{-1} and 1600cm^{-1} can be assigned to in-plane bending of the N – H bonds of the peptides. Also well pronounced are C – H_2 waging vibrations between 1420cm^{-1} and 1500cm^{-1}. The intensities of the region between 1200cm^{-1} and 1360cm^{-1} result from various C – H deformations, centered at 1297cm^{-1} as well as C – N bending modes, centered at 1267cm^{-1} referred to as amide III. The small peak centered around 1095cm^{-1} can be assigned to symmetric stretching of phosphorous groups of molecules such as ATP or RNA. Also very typical for spectra of cells or biological material in general, the sharp peak at 1002cm^{-1} attributed to the a_{1g} all symmetrical vibration of the phenyl group of phenylalanine, which contributes roughly 4% to the overall amino acid contents of the cell. The region below 1000cm^{-1} is usually less characteristic. The peak at 716cm^{-1} has

not been assigned so far. Shape and appearance of the peaks are very distinct and vary only little throughout the cytoplasm.

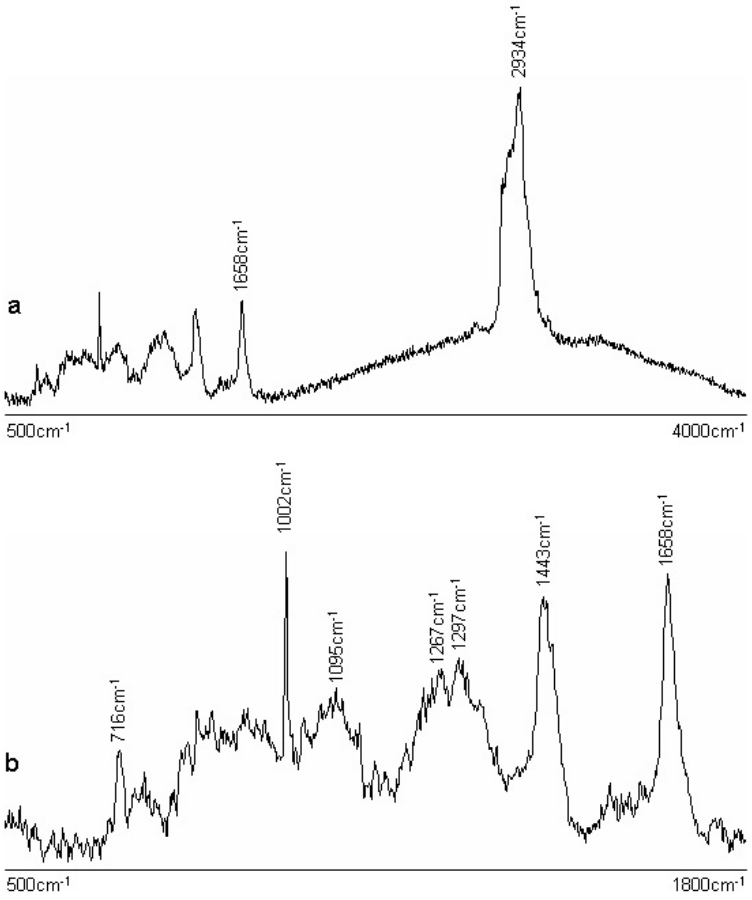

Figure 3.2.1.: Raman spectrum from within the cytoplasm. Plot **a** shows the whole spectral range from 4000cm^{-1} to 500cm^{-1}, **b** shows the main protein features between 1800cm^{-1} and 500cm^{-1}.

Figure 3.2.2. shows spectra from within the nucleus and the nucleoli. Again, plots 3.2.2.a1 and 2 show the whole spectral region, whereas 3.2.2.b1 and b2 show the region between 1800cm^{-1} and 500cm^{-1}. The spectra of nucleus and nucleoli are very similar with only little relative intensity variations. The protein peaks are still the predominant

features in the spectra. The C – H stretching region is again centered at 2934cm^{-1}. The amide I and C – H_2 deformations are found pretty close to the positions found in the cytoplasm at 1657cm^{-1} and 1448cm^{-1} respectively. The centers of the C – H deformation and amide III region have shifted quite a bit from 1297cm^{-1} to 1325cm^{-1} and 1267cm^{-1} to 1257cm^{-1}. Apparently, the whole appearance or shape of that spectral region between 1190cm^{-1} and 1380cm^{-1} is different compared to the spectra of the cytoplasm. The same statement can be made with respect to the shapes of the C – H stretching, amide I and C – H_2 waging bands, which will be discussed in detail in the following chapter. In addition to the protein peaks, some DNA/RNA bands can be assigned. The strong peak at 1575cm^{-1} results from a stretching of the double bonds of the purine bases of adenosine and guanosine. The intensity of the symmetrical P – O stretching of the PO_2^- groups at 1095cm^{-1} increases due to the vibration of the phosphate ester backbone of DNA and RNA. Also well pronounced is apparently the band at 785cm^{-1}, which has been assigned to the pyrimidine ring breathing of cytosine, thymine and uridine. All other DNA/RNA features merge with the protein spectra or cannot be clearly assigned at the given noise level.

The signal quality was generally satisfactory, but varies greatly from nucleus to cytoplasm. In mammalian cells, approximately 80% of the cell body consists of the nucleus. For adherent cells, the remaining 20% of cytoplasm that grows onto the substrate can get very thin. The cell also looses parts of its water contents due to fixation and drying. An estimated value for the thickness of the nucleic region is 5µm whereas the cytoplasm may be 2µm or less. The signal to noise of spectra form the nucleus versus the cytoplasm may vary by a factor ten. The signal quality may also vary from cell to cell.

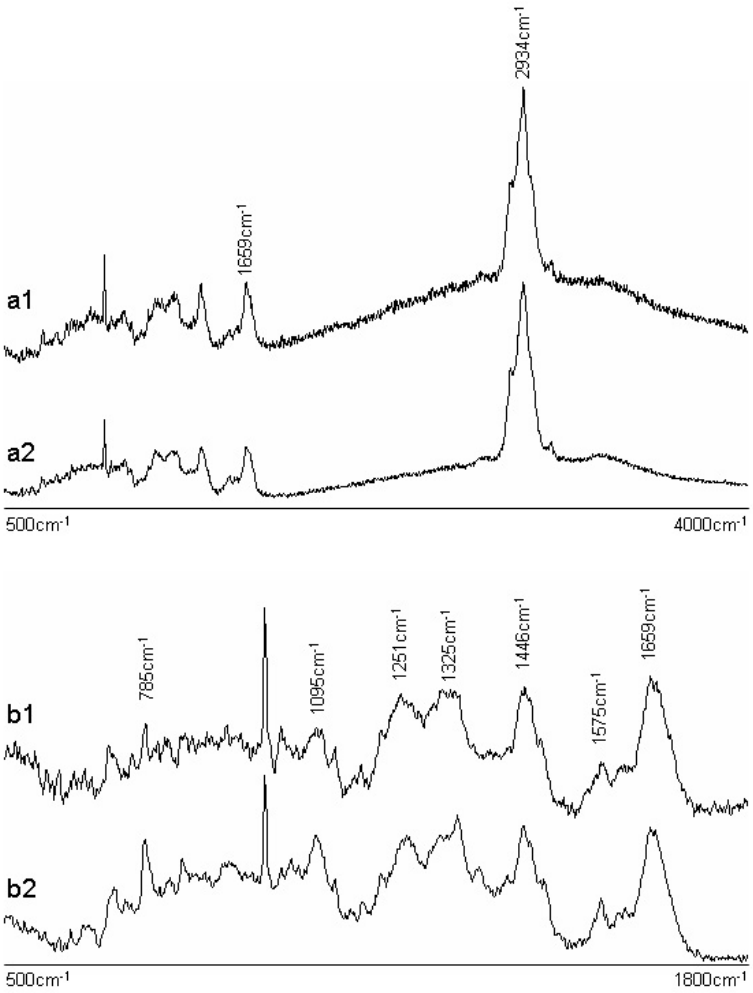

Figure 3.2.2.: Raman spectra from within nucleus (a1, b1) and nucleoli (a2, b2)

The protein features generally dominate the spectra form within the nucleus and nucleoli since the DNA/RNA content is still small. Estimated protein:RNA:DNA for nucleus and nucleoli are 100:10:1 and 100:25:1 respectively.[9, 27, 28] Figure 3.2.3.b1-b3 shows images reconstructed from the absolute intensities of the pyrimidine ring breathing at 785cm^{-1}. The images reproduce the location of the nucleoli but fail to contrast the nucleus from the surrounding cytoplasm.

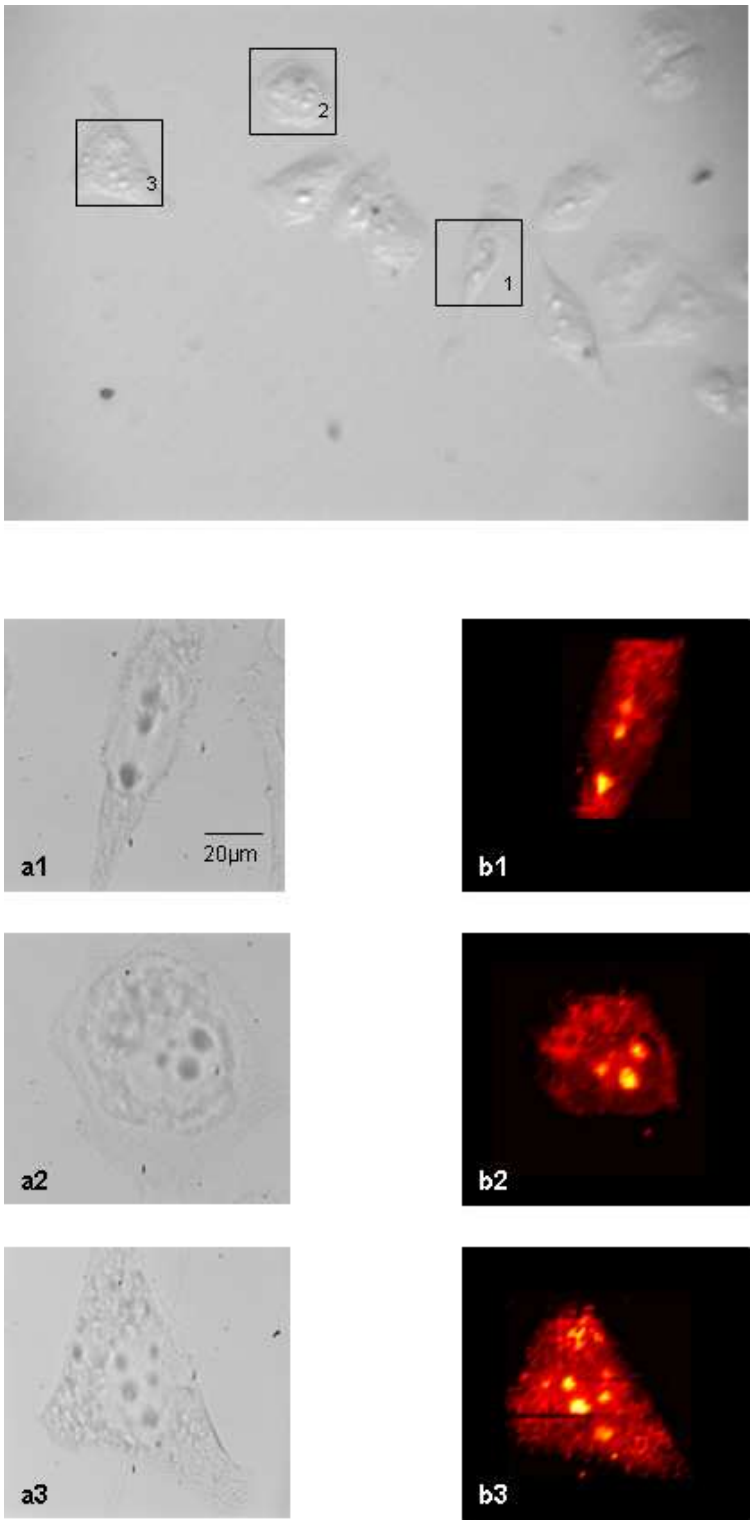

Figure 3.2.3.: Microscopic images and Raman images reconstructed from the pyrimidine ring breathing at 785cm^{-1}

Given the fact that the DNA/RNA features are far less pronounced than the protein features the results may not be surprising. The DNA and RNA concentration within the cytoplasm is too small to be detected.

Figure 3.2.4.a1-a4 show HeLa cells undergoing the typical stages of mitosis. During mitosis or M-phase the chromatin of the cell is rearranged to result in two individual nuclei. In the prophase the chromosomes become visible and start aligning along the spindle of the cell. After alignment (metaphase) the replicated sets of chromosomes are driven apart towards the poles of the cell (anaphase). In the telophase cytokinetics is almost over and the nuclei are being formed. The fluorescence stained images d1-d4 show the chromatin distribution using the DNA specific fluorescence dye 4,6- diamidino- 2- phenylindol (DAPI). The chromatin is most condensed during meta- and anaphase. The Raman images b1-b4 were reconstructed from the overall intensity of the 785cm^{-1} DNA band. All DNA Raman features appeared to be most intense during meta- and anaphase. For both phases, the DNA Raman band intensities reproduce the chromatin distribution with great specificity. Interestingly, this is not the case for the pro- and telophase. As the comparison with the fluorescence images shows, the DNA Raman intensity plots do not reflect the chromatin distribution correctly. The shape of the cell body can be easily reproduced by plotting any of the protein peaks as shown in figures c1-c4.

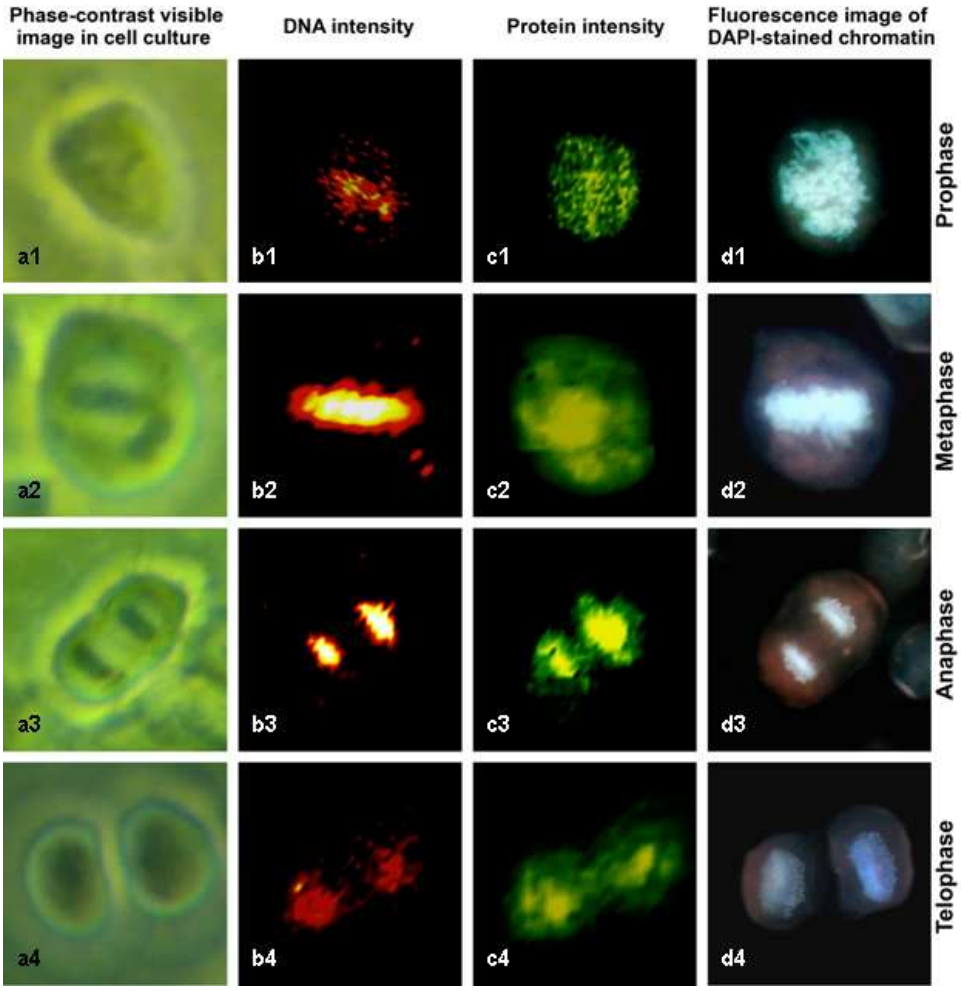

Figure 3.2.4: Photographs, Raman and fluorescence (DAPI stain) images of HeLa cells during various phases of mitosis. (top row) prophase, (2nd row) metaphase, (3rd row) anaphase, (bottom row) late telophase. All images are collected at 40X magnification. (Column 1) Phase-contrast images of live cells in culture. (Column 2) Raman scattering intensity plots for the DNA scattering intensities at $785cm^{-1}$. The colors range from black (low intensity) to red to white (high intensity). (Column 3) Raman scattering intensity plots for the protein scattering intensities at $1650cm^{-1}$. The colors range from black (low intensity) to green to yellow (high intensity). (Column 4) Fluorescence images of the DAPI-stained cells.

3.2.2. Discussion

The images reconstructed from the Raman data are of great specificity contrasting the chromatin against the cytoplasm for the meta-, and anaphase as well as for localizing the nucleoli of the cells not in the M-phase. Apart from that, the low intensity of the DNA bands found inside the nuclei of the non dividing cell, the prophase and the probably late telophase are interesting. There may be two possible explanations. First, the distribution of the DNA is not homogeneous. This may explain why in some regions, at least at the observed signal quality, no DNA is detectable. Furthermore, the intensity of the peaks may depend on the overall structure or density of the chromatin. Since there is a correlation between the chromosomal arrangement and the protein/DNA ratio during the different stages of mitosis this assumption seems to be reasonable. The protein/DNA packing ratio of the chromatin complexes for a cell not in mitosis is on the order of 40, as compared to a metaphase chromosome with a packing ratio of 10,000. Thus, the chromatin may be too diffuse to yield detectable Raman scattering signal in the volume probed in Raman microscopy, which is on the order of $1\mu m^3$, or about 10^{-12}g. For the Raman scattering the overall density of the scattering material is probably the most crucial factor. During mitosis, the DNA/histone system is in its most condensed form, which may increase the signal intensities of the DNA. Arguments about intensity variations in correlation with chromatin density have been introduced to explain similar observations employing IR-microscopy.[29, 30] Correlation between Raman scattering intensities and the chromatin packing may have potential applications to distinguish the individual stages within the cell cycle of proliferating cell.

3.3. Cluster Analysis

3.3.1. Results

A similar comparison of the band shapes based on hierarchical clustering was performed for the spectral regions of the C – H stretching vibrations from 2800cm^{-1} to 3100cm^{-1}, the amide I band between 1525cm^{-1} and 1750cm^{-1}, the C – H_2 waging deformations from 1400cm^{-1} to 1525cm^{-1} as well as for the amide III region between 1175cm^{-1} and 1375cm^{-1}. All spectra were smoothed using the Savitzky-Golay procedure with nine points. To avoid clustering artifacts from sample thickness, the spectra were vector normalized over the amide I band for the lower wavenumber region and from 2800cm^{-1} to 3100cm^{-1} for the analysis of the C – H stretching bands. The results for all four regions are shown in Figure 3.3.1. The first row of false color maps depicts the number of clusters needed to image the location of the nucleus in which the number of colors equals to the number of clusters. For all spectral regions only three clusters are sufficient to contrast the nucleus against the cytoplasm. The location of the nucleus is reproduced best by clustering in the amide III region. To get a more detailed image, a higher number of clusters or lower level of similarity was employed to reconstruct the maps of the second row. The C – H stretching as well as the amide I region reproduce the location of the nucleoli with great specificity. Clustering over the C – H_2 waging and amide III bands does not fail to localize the position of the nucleoli, but give a fuzzier image. The most detailed image results from the C – H stretching region. Clearly regions from the cytoplasm start to differentiate. The direct vicinity of the nucleus falls into a different cluster than the bulk of the cytoplasm. In addition, the nucleic region appears not to be homogeneous.

In order to test the reproducibility of the cluster analysis and to find out what region would be most analytical, the clustering was performed on more than one cell. Figures 3.3.2. and 3.3.3. show the results for two other cells. Again the spectra where smoothed employing the Savitzky-Golay procedure using nine points and vector normalized over the amide I or C – H stretching bands. As in the previous example, only three clusters are needed to image the nucleus of the cells. In most of the cluster images, size and location of the nucleus correspond very well with the light microscopic images. The clustering of the C – H stretching region slightly underestimates the size of the nucleus of the second cell whereas the clustering of the amide I band overestimates its size. To image the position of an average of six clusters were needed for all spectral regions employed. The best results were obtained for the amide I and C – H_2 deformation bands.

3.3.2. Discussion

In general, the images of the cluster analysis are in good agreement with the microscopic images. As to be expected, the greatest contrast in the similarity of the spectra lies between the cytoplasm and the nucleic region. Imaging the nucleoli was usually achieved by plotting an adequate number of clusters. The particular biomolecular composition of the respective cellular compartments was found to be represented in the band shapes of all four spectral regions that were chosen. The most reliable region reconstructing the position and shape of the main cellular features, especially the

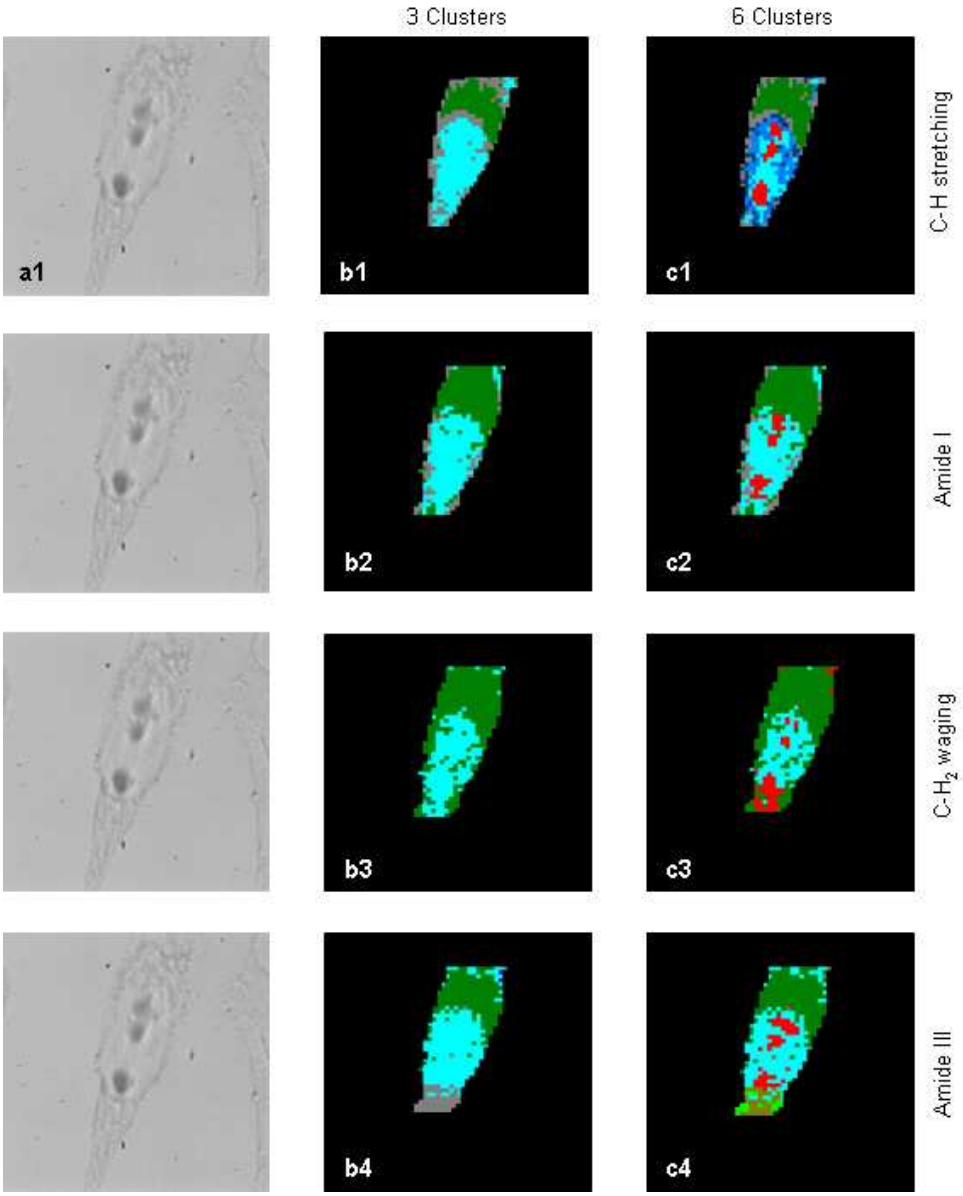

Figure 3.3.1.: Pseudo-color maps from the hierarchical cluster analysis (HCA) for the C – H stretching region 2800 – 3100cm^{-1} (b1, c1), amide I 1525 – 1750cm^{-1} (b2, c2), C – H_2 waging deformations 1400cm^{-1} to 1525cm^{-1} (b3, c3), and amide III 1175cm^{-1} and 1375cm^{-1} (b4, c4). Column 2 uses three clusters, the minimum to distinguish the nucleus. Column 3 uses six clusters, where the nucleoli become apparent.

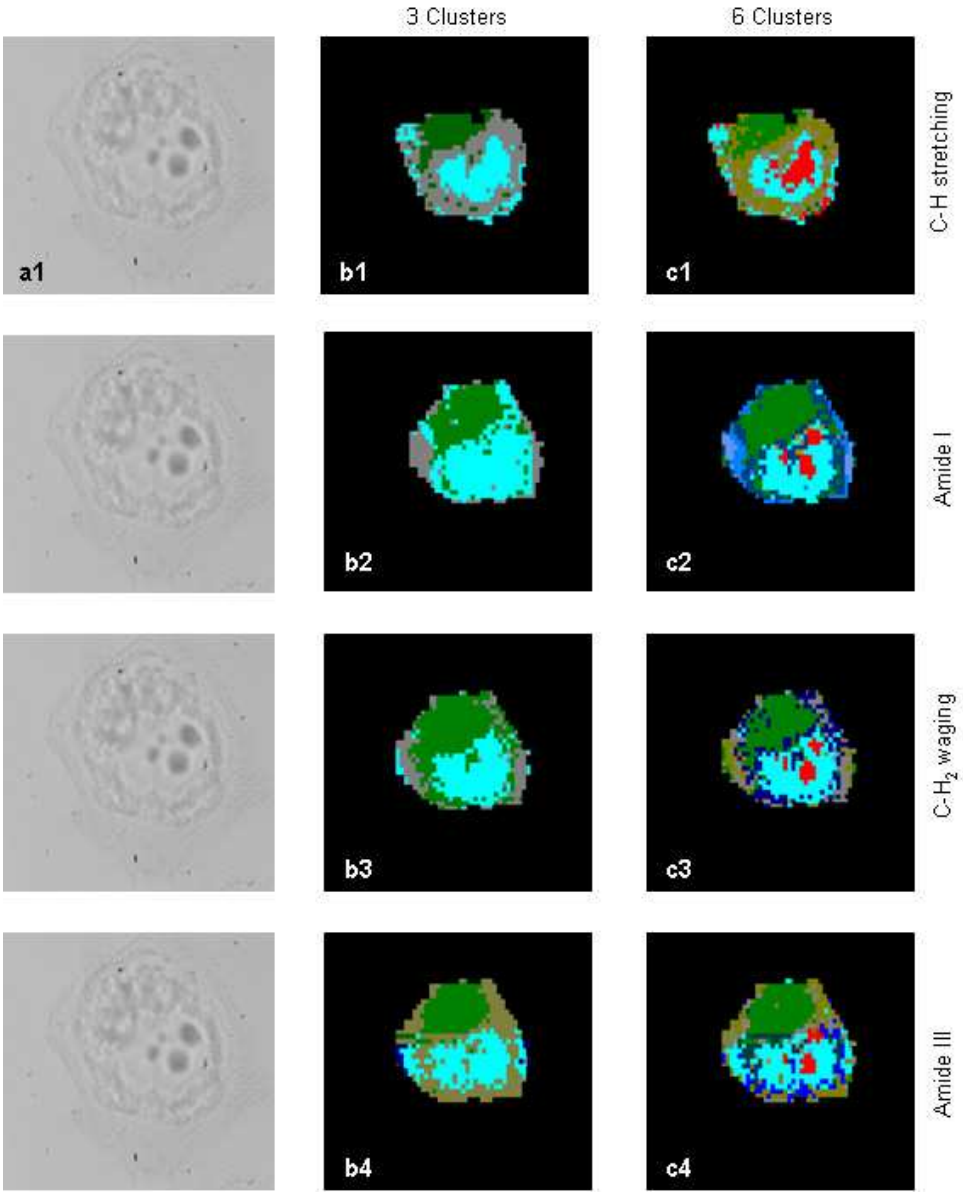

Figure 3.3.2.: Pseudo-color maps from the hierarchical cluster analysis (HCA) for the C – H stretching region 2800 – 3100cm^{-1} (b1, c1), amide I 1525 – 1750cm^{-1} (b2, c2), C – H_2 waging deformations 1400cm^{-1} to 1525cm^{-1} (b3, c3), and amide III1175cm^{-1} and 1375cm^{-1} (b4, c4). Column 2 uses three clusters and column 3 uses six clusters.

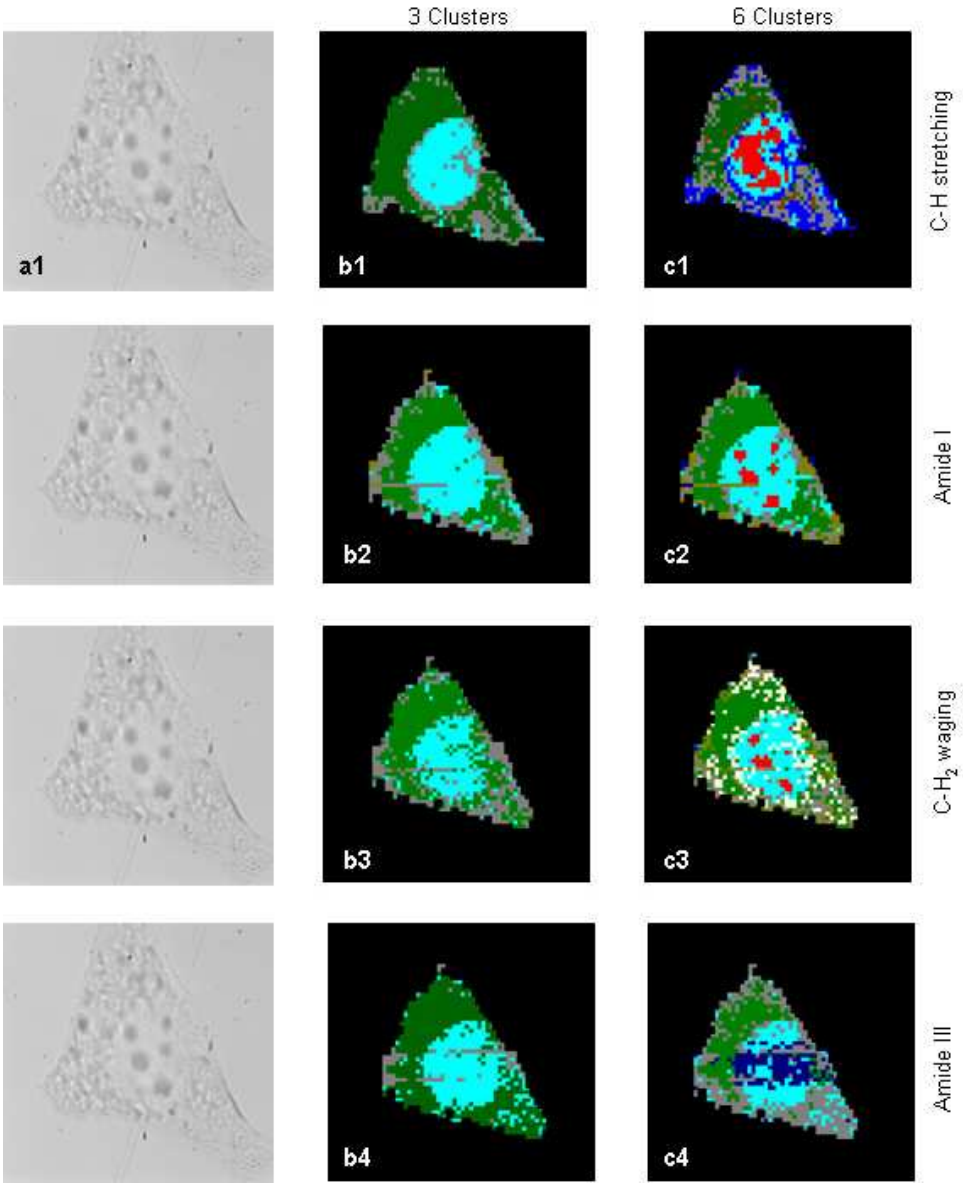

Figure 3.3.3.: Pseudo-color maps from the hierarchical cluster analysis (HCA) for the C – H stretching region 2800 – 3100cm^{-1} (b1, c1), amide I 1525 – 1750cm^{-1} (b2, c2), C – H_2 waging deformations 1400cm^{-1} to 1525cm^{-1} (b3, c3), and amide III1175cm^{-1} and 1375cm^{-1} (b4, c4). Column 2 uses three clusters and column 3 uses six clusters.

nucleoli, proved to be the amide I region. By simply looking at the spectral features, particularly comparing the spectra from figures 3.2.1. and 3.2.2. one would expect the amide III region to be the most analytical. However, considering the signal to noise ratio of both regions, the amide I band is apparently the region of greater signal quality since its intensity is at least twice as high. Noise can be generally seen as the main source of inaccuracy of the cluster analysis. As mentioned before, the signal quality can vary by a factor ten due to the inhomogeneity of the sample thickness. The fact that the cluster analysis not always delineates the nucleus/nucleolus features can also be attributed to the relatively small number of spectra. Cluster analysis works best for large data sets and high signal to noise ratios. For the employed experimental setup between 500 and 1000 spectra can be collected per cell. The number of spectra could be greatly increased, by a factor four, if the apparatus was not limited by the step size of the x,y- microscopic stage, but allow data collection of the spatial resolution of the laser light.

However, the clustering shows some remarkable results in that it recognizes the main cellular features, which was not possible based on single wavelength analysis. With improved spatial resolution, one could also expect further differentiation of regions within the cytoplasm, which has a promising outlook.

Chapter 4: Drug distribution inside cells

4.1. Introduction

The possibility to image subcellular compartments at a 1µm spatial resolution or less offers some interesting applications. One obvious question is to what extent one can use Raman microscopy to image the distribution or uptake of biologically active substances. Controlled by diffusion endocytotic processes and various transport mechanisms, small molecules or larger ones such as polypeptides or carbohydrates pass the membrane. There is active transport, where molecules are pumped in and out transforming energy, as well as passive transport go through a channel with the gradient. Provided that the uptake is great enough it may be possible that the targeted molecules yield sufficient signal. One major advantage would be the spectral information, which allows speculation about the chemical integrity or modification of a substance as well as conformational changes. Many substances are metabolized inside the cell such that the product structure differs from the original chemical. Often those chemicals are either activated or inactivated due to metabolic activity. Raman spectra would provide important experimental evidence whether a certain compound changes its chemical composition upon uptake. Also interesting are conformational changes of active compounds, especially peptides, at their binding sides. Numerous spectroscopic data of solution studies can be found in the literature. Raman microscopy would allow evaluating data measured on isolated structures in solution against real-world experiments inside a living cell organism.

One major field of interest evaluating bioactivity is the search for new lead compounds for chemotherapy. Some 100000 compounds a year are screened for potential anti cancer activity. The first step in the screening process is usually the evaluation of the cytotoxicity against various cell lines of certain types of cancer. A number of toxicity parameters such as IC_{50} (inhibitory concentration, 50%) or LD_{50} (lethal doses, 50%) values, have been established for those *in vitro* studies. Usually the dose for which half of the cell population is affected is determined. An estimated amount of perhaps 2% of the screened compounds shows results promising enough to be passed onto animal studies, where the number is again greatly reduced. Out of 74196 compounds screened by the NCI in 1997 only 5 qualified for clinical trials.[31] Any information about the mode of action of potential substances is of great importance to increase the number of qualifying agents.

The most critical aspect applying Raman microscopy to the above issues is the detection limit of the relatively weak Raman effect. Experiments in solution are usually not accomplished at less then millimolar concentrations. IC_{50} values are normally on the order of micro-mols or less. Even at, from a pharmaceutical viewpoint, rather high concentrations of 100µM conventional Raman spectroscopy is at least one order of magnitude away from the desired sensitivity. In order to detect sufficient signal it seems necessary that a substance accumulates inside the cell or inside certain cell compartments to a great extent. For what type of compounds and for how many this may be the case is difficult to estimate. Most promising may be DNA targeting molecules with high binding efficiencies. DNA targeting drugs often bind to either the major or the minor groove of the helix or intercalate somewhere between the base pairs. In solution binding

efficiencies reach up to 90% which suggests a great potential for accumulation inside the nucleus. Once bound to the DNA replication, topoisomerases, and other enzymatic activities are hindered.

Previous experiments have shown that it is indeed possible to detect DNA binding structures inside cells using conventional Raman spectroscopy.[32] The deployed agent belongs to the minor groove binding family and consists of a bisbenzimidazole core structure with head and tail side functionalities that twist the molecule to fit into the minor groove. Those promising results were inspiring to systematically test other DNA binding systems. The most evident approach was testing derivatives of the bisbenzimidazole structure that had been subject to cytotoxicity experiments. Furthermore it was interesting whether other well known groove binders such as Distamycin can be detected. As intercalating systems actinomycin D, amsacrine, acriflavine, camptothecin and benzopyrene derivatives were chosen. The first two are established chemotherapeutic agents whereas benzopyrenes are DNA damaging compounds that cause cancer.

Another way of approaching the sensitivity issue lays is the scattering intensities of the individual vibrational modes. Isolated vibrations with strong intensities are certainly more suitable. An ideal functionality is the cyano group. Its frequency appears within a spectral region where there are no protein bands and it has usually exceptionally strong intensities. There are a number of cyano group containing anti-neoplastic agents described in the literature. One can roughly divide them into three families. Cyanoguanidine compounds, cyanocarboxamine-aziridines, and the leflunomid (LFM)

family. All of them have different mode of actions and none of them shows particular affinity for DNA.

In the following, the results for the individual compounds are presented. Almost all of the tests were performed on the HeLa cell line or lymphoma cells. The self adherent HeLa cells have the advantage that the main cellular features can be clearly distinguished without complicated staining techniques. Also the cytoplasm is relatively large. Hence, distribution issues can be addressed in greater detail, although the cytoplasm gets very thin which causes the signal quality to decrease drastically. Lymphoma cells are suspended cells that give generally better signal due to their spherical shape, unfortunately they show less cellular features.

The results are first discussed for each individual group of compounds and compared in the following discussion section.

4.2. Experimental

Cells were grown as previously described. Cytotoxins were added to the growth medium from refrigerated stock solutions. Substances which were not sufficiently water soluble were administered from solutions in 100% dimethylsulfoxid (DMSO) to reach the desired concentration, not exceeding a final DMSO concentration of 1%. Hoechst 33258, actinomycin D, amsacrine and acriflavine were purchased from Sigma-Aldrich (Milwaukee, WI). Camptothecin was available from Calbiochem (La Jolla, CA). The benzopyrenes were kindly provided from Professor Lakshman at City College – New York. All other compounds were synthesized as described in the Chemistry sections. Cells were treated at IC_{50} concentrations found in the literature. Inoculation times varied,

depending on the compound used. In the case, no spectral changes could be detected after inoculation overdoses up to 100 fold were applied. Different exposure times with usually 1h distance were tested. All cells were fixed after exposure and dried with compressed air.

4.3. Bisbezimidazoles

Bisbenzimmidazole derivatives are well known for their DNA binding activity. The planar benzimidazole groups bind into the minor groove of the double helix forming hydrogen bonds specifically at AT sequences. As minor groove binders bisbenzimidazoles exhibit cytotoxic and anti-tumor activity. Lead compound for the search for chemotherapeutic agents has been a substance known as Hoechst 33258 (**1**) which was introduced as a fluorescent stain for chromosomal analysis. The compound slows DNA replication and prolongation of the G2 phase of the cell cycle. It has been tested for chemotherapeutic potential in clinical trials phase II.[33]

In order to enhance the efficiency of Hoechst 33258 various derivatives have been synthesized and evaluated against the lead structure. One common approach to increase the toxicity of potential structures is to attach DNA alkylating groups. Very common here are derivatives of mustard agents such as chloro-diethyl-amines (**2**) which form covalent bonds with nitrogen of the nucleic bases. Bielawski et. al. modified the Hoechst 33258 structure by attaching chloroalkyl and bromoalkyl moieties to its phenoxy-functionality. They report an increased binding affinity for DNA and an increase in cytotoxicity against a breast cancer cell line.[34] Another approach to further investigate the binding nature of

Hoechst compounds was testing derivatives of the symmetric version of its bisbenzimidazol core structure, which also showed a promising increase in cytotoxicity up to two orders of magnitude with respect to the IC_{50} values.[35]

To further investigate the potential of Raman spectroscopy to image the uptake of cytotoxins two chloroalkyl-carbamate derivatives (**3**, **4)** and one symmetric dibenzimidazole (**5**) were synthesized.

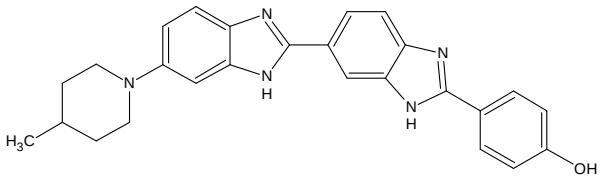

1

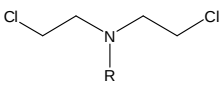

2

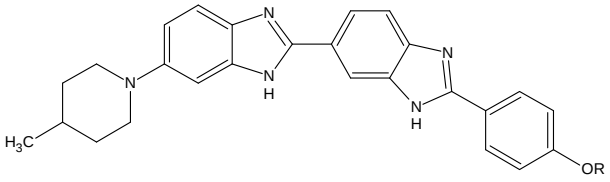

3 R =

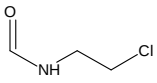

4 R =

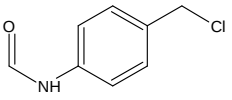

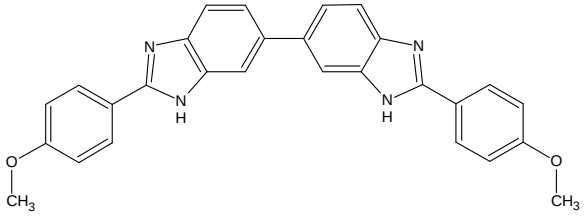

5

4.3.1. Results

A spectrum of 10mg/ml Hoechst 33258 in aqueous solution is shown in figure 4.3.1. Very characteristic are the C=C and C=N stretching features of the benzimidazole moieties at 1554cm^{-1}, 1575cm^{-1} and 1610cm^{-1}, 1634cm^{-1} respectively. One may assume that the peaks of higher intensities and lower wavenumbers originate from the benzimidazole next to the piperazine ring, because of an increased electron density due to electron donation from the nitrogen. The 979cm^{-1} band can possibly be associated with the ν_1 a_{1g} ring breathing of the phenol group, which is usually well pronounced for phenyl derivatives. All other peaks are more difficult to assign.

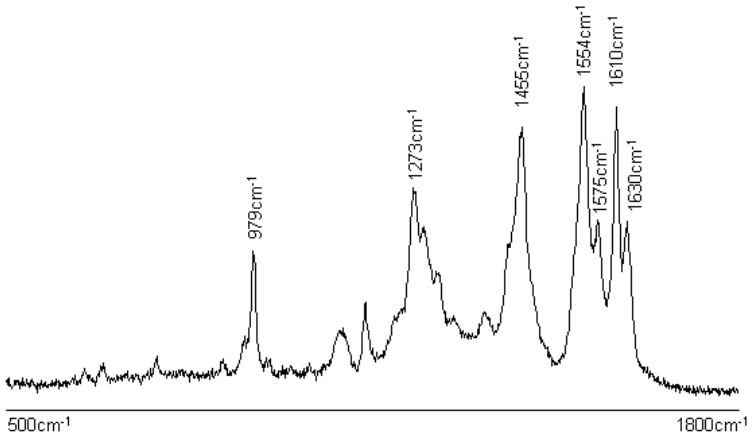

Figure 4.3.1.: Raman spectrum of Hoechst 33258 in aqueous solution [10mg/ml]

Figure 4.3.3. a1-5 shows HeLa cells inoculated with Hoechst 33258 at a concentration of 50µM for 30min (a1-2) and 2h (a3). IC_{50} values reported in the literature range from 9.5µM (96h exposure) for ovarian cell lines[36] to 67 ± 2µM (48h exposure) for breast cancer cells[34]. Compared to untreated HeLa cells the degradation of the cells is clearly discernible. The nuclei as well as the nucleoli are less differentiated and the cells loose their affinity for the substrate. At the chosen concentration of 50µM, 100% of

the cells showed similar abnormalities after 30min, indicating that 50μM is well above the IC_{50} tolerance for HeLa cells. After 2h, only 20% of the cells remained attached to the substrate showing further degenerated features.

Figure 4.3.2. shows a spectrum from within the nucleus, which represents an area of high concentration. The spectra from within the cell appear to be more or less a superposition of the spectrum of the compound and a typical cell spectrum. The peak positions of the characteristic C=C and C=N stretching modes do not vary by more than a few wavenumbers. There are also no particular changes in the relative intensity appearance of those peaks. The amide I band is still around $1665cm^{-1}$. The protein C – H bending region between $1500cm^{-1}$ and $1425cm^{-1}$ and the amide III region are now dominated by the peaks of the Hoechst compound at $1455cm^{-1}$ and $1237cm^{-1}$. There are intensity variations of the benzimidazole peaks with highest intensities around the nucleoli. However, the spectral features were found throughout the whole cell body. Although the compound has a high affinity for DNA it apparently does not exclusively accumulate inside the nucleus. For a substance that is commonly used for chromosomal analysis this may be surprising. However, standard protocols for Hoechst staining procedures are applied after cell fixation which may be crucial for its application.

The images 4.3.3. b1-b5 are reconstructed from C=C stretching Raman intensities between $1530cm^{-1}$ and $1590cm^{-1}$. The overlaid pictures c1-c5 show the distribution of the compound inside the cell. Because of its high affinity for DNA the compound accumulates inside the nucleus more than in the cytoplasm. After two hours the accumulation extends all over the cell body.

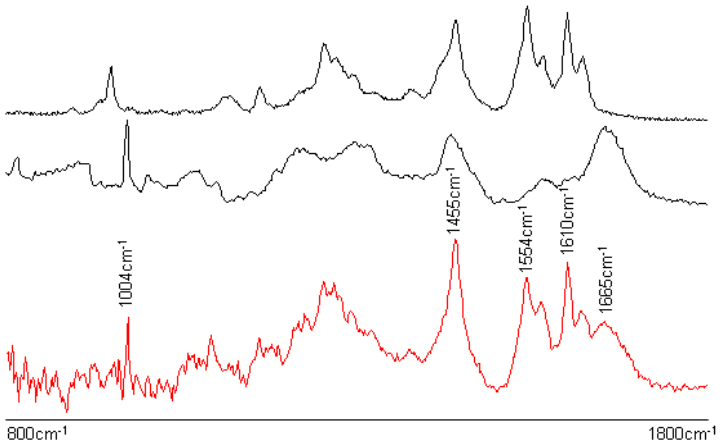

Figure 4.3.2.: Raman spectrum from areas with high concentration of Hoechst 33258 (bottom) in comparison with a spectrum of the pure compound (top) and a typical spectrum from the cytoplasm of an untreated cell (middle)

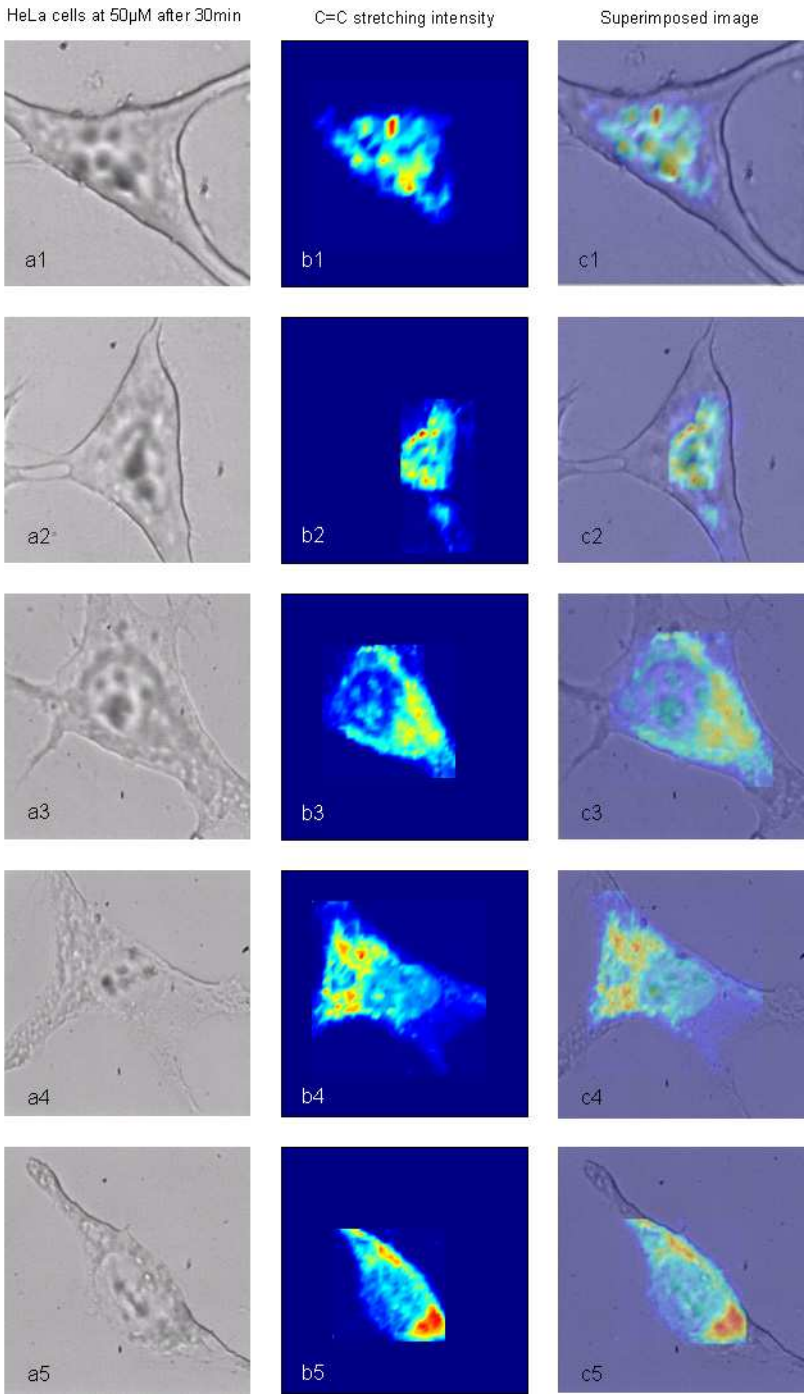

Figure 4.3.3.: Microscopic pictures of HeLa cells treated with Hoechst 33258 at 50µM for 30 min (a1-5) . Images b1-5 are reconstructed from C=C stretching Raman intensities between1530cm^{-1} and 1590cm^{-1}. The overlaid images c1-5 show the distribution of the compound inside the cells.

We now turn to the results of the bisbenzimidazole derivatives. The Raman spectra of the derivatives with alkylating functionalities (**3**, **4**) were very similar to the Raman spectrum of the Hoechst structure. Neither the carbon – chlorine stretching modes nor any of the phenyl vibrations of the 2-chloroethyl-phenyl derivative have pronounced Raman intensities. HeLa cells treated at a concentration of 50μM showed similar sensitivity and the analysis of the spectral parameters and the drug distribution were no different than for the original Hoechst compound.

HeLa cells were less sensitive against inoculation with the symmetric bisbenzimidazole **5**, which is in contrast to cytotoxicity experiments on ovarian cell lines.[35] Cells were treated with concentrations between 50μM and 100μM administered from 10mg/ml DMSO stock solutions. After 10h for 50μM and 2h for 100μM approximately half of the cells were detached from the substrate and cells still attached showed similar signs of degradation. However, no spectral changes were detectable at any concentration or time. Spectra of cells incubated with **5** did not show any additional peaks or substantial derivations from spectra of cells that were not treated. Given that both structures are chemically related the results are surprising. Both compounds have similar cytotoxicity parameters.[35] The minor groove binding activity has been well established and crystallographically characterized.[36] Molecular modeling also suggests similar binding affinity for both structures.[37] It is possible that the compounds although chemically related may have different biochemical properties and different bioactivity. Therefore the amount that accumulates inside the cell may be much less for the symmetric derivative and hence not detectable. One indication may be the great contrast in water solubility. The symmetric bisbenzimidazole is almost not soluble in water and

the inoculation *in vitro* has to be administered from DMSO stock solutions. Although, in this case the presence of a low percentage of DMSO in the culture medium rather supports the uptake of the compound since it increases the susceptibility of the cell membranes.

To further elucidate the possibilities to monitor the uptake of minor groove binding systems similar experiments were carried out with distamycin which also gave negative results.

4.3.2. Chemistry

The carbamate derivatives of Hoechst 33258 were synthesized by simple addition of an appropriate isocyanate at the phenol function of the core structure. (scheme 1).[34] The symmetric bisbenzimidazoles are accessible via a condensation of 3,3',4,4'-tetraamino-biphenyl with benzaldehydes in the presence of nitrobenzene (scheme 2).[35]

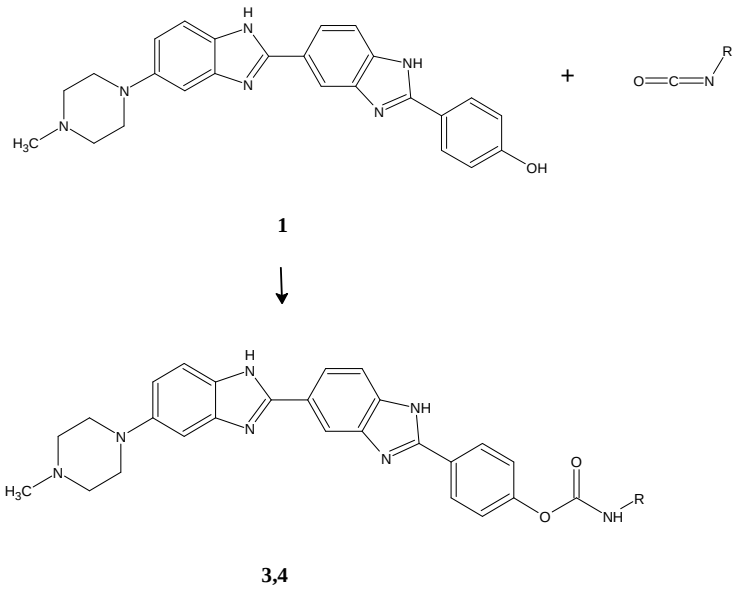

Scheme 1: Synthesis of the carbamates

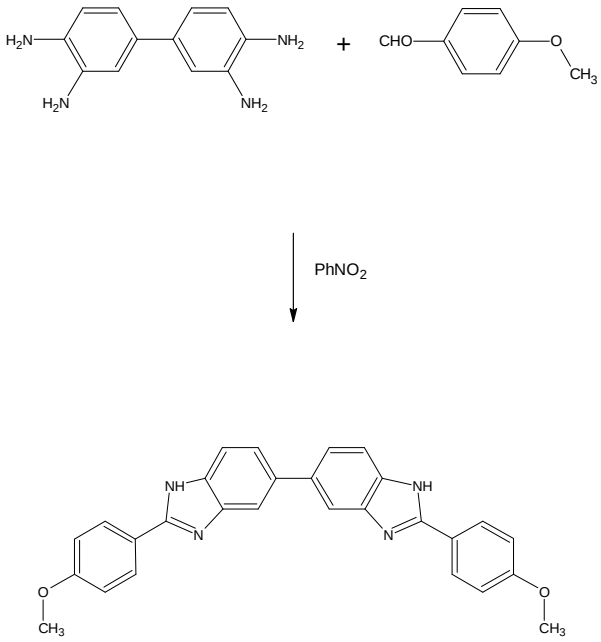

5

Scheme 2: Synthesis of symmetric bisbenzimidazoles

2-[2-(4-((2Chloroethyl-)carbamoyloxy)phenyl)-6-benzimidazolyl]-6-(1-methyl-4-piperazinyl-)benzimidazole: 500mg (0.93mMol) of Hoechst 33258 were dissolved in 25ml anhydrous DMF. 5.2ml *N,N*-diisopropyl-ethylamine and 1.31ml (18mMol) of 2-chloroethyl-isocyanate were slowly added. The mixture was stirred for 27h. The solvent was distilled under reduced pressure at 60-80˚C and the product with ethylacetate/methanol (1:1) chromatographically purified.

^{1}H-NMR (400MHz) (DMSO-d_6): δ = 8.68 (s, 1H, Ar-H), 8.30 (d, 2H, Ar-H), 8.25 (d, 2H, Ar-H), 7.88 (d, 2H, Ar-H), 7.72 (d, 1H, Ar-H), 7.32 (d, 1H, Ar-H), 7.21 (s, 1H, Ar-H), 7.17 (d, 1H, Ar-H), 3.58 (t, 2H, -CH_2-Cl), 3.35 (m, 4H, N-CH_2-), 3.14 (m, 2H, N-CH_2-), 2.86 (m, 4H, N-CH_2-), 2.75 (s, 3H, N-CH_3)

2-[2-(4-((4-Chloromethylphenyl-)carbamoyloxy)phenyl)-6-benzimidazolyl]-6-(1-methyl-4-piperazinyl-)benzimidazole: As above using 2.763g of 4-chloromethyl-phenyl-isocyanate.

^{1}H-NMR (400MHz) (DMSO-d_6): 8.65 (s, 1H, Ar-H), 8.29 (d, 2H, Ar-H), 8.23 (d, 2H, Ar-H), 7.86 (d, 2H, Ar-H), 7.71 (d, 1H, Ar-H), 7.56 (d, 2H, Ar-H), 7.45 (d, 1H, Ar-H), 7.30 (d, 2H, Ar-H), 7.20 (s, 1H, Ar-H), 7.16 (d, 1H, Ar-H), 4.74 (s, 1H, -CH_2-Cl), 3.60 (m, 4H, N-CH_2-), 3,10 (m, 4H, N-CH_2-), 2.63 (s, 3H, N-CH_3)

2,2-Bis-(4'-methoxyphenyl-)-5,5-bi-1*H*-benzimidazole: 2,14g (10mMol) of the tetramine and 2.72g (20mMol) of the p-anisaldehyde were dissolved in 30ml nitrobenzene and heated between 150-200˚C for 16h under Argon. 50ml of hexane were added to the cooled solution and the resulting precipitate with silica gel chromatographically purified.

^{1}H-NMR (400MHz) (DMSO-d_6): δ = 8.29 (d, 4H), 7.71-7.81 (m, 6H), 7.56-7.70 (m, 4H), 3.85 (s, 6H)

4.4. Actinomycin D

Actinomycin D (**6**) is one of many biologically active molecules extracted from the *streptomyces* species. Introduced in 1957, it was the first antibiotic to be used in cancer treatment.[38] Although the substance is highly toxic, causing severe side effects it has been applied against a variety of tumors such as kidney, germ cell and bone tumors. Actinomycin D belongs to the phenoxazine/phenoxazone family with a phenoxazone chromophore and two identical penta-peptide lactone rings. The planar phenoxazone core

intercalates into the DNA base pairs, preferably between GpC sequences while the penta-peptide rings rest in the minor groove. Actinomycin D also interacts with single stranded DNA as well as RNA, which may contribute to its toxicity.

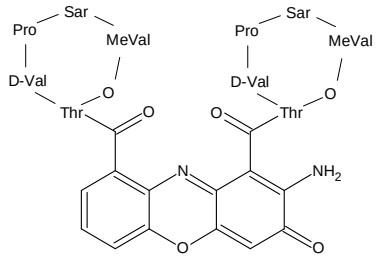

6

4.4.1. Results

The Raman spectrum of actinomycin D shown in figure 4.4.1. is dominated by the skeleton vibrations of the phenoxazone moiety of the molecule between 1200cm^{-1} and 1600cm^{-1}. The C – H bending modes of the cyclic oligopeptide residues may also contribute to the intensities around 1456cm^{-1}. The carbonyl stretches appear around 1635cm^{-1}. The spectrum shown is in good agreement with previously reported resonance Raman and pre-resonance Raman spectra in methanol solution.[39, 40] Based on Raman excitation profiles the following bands have been assigned. The two most intense bands at 1502cm^{-1} and 1481cm^{-1}result from the C – C=N and C – C=C asymmetrical stretching modes, whereas the symmetrical vibrations appear at 1263cm^{-1} and 1213cm^{-1} respectively. The bands at 1454cm^{-1} is associated with a ν_{19} phenyl deformation. The other strong intensity at 1402cm^{-1} has been assigned to a C – NH_2 bend. The main differences to the spectra in methanol solution are additional peaks at 1591cm^{-1}, 1573cm^{-1} and 1555cm^{-1} as well as 1425 cm^{-1} and 1238cm^{-1} which could either arise from conformational changes or the penta-peptide lactone rings, which are out of resonance for the excitation wavelengths employed in the previous studies.

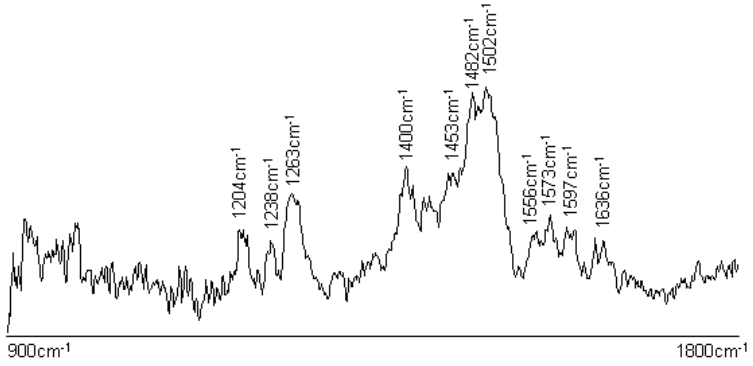

Figure 4.4.1.: Raman spectrum of solid actinomycin D

Figure 4.4.4. a1-a5 shows HeLa cells treated with 10µM actinomycin D for 20h which is within the effective range of concentration for *in vitro* experiments. The nuclei of the cells are still in shape whereas the cytoplasm seemingly looses its density. The nucleoli are no longer visible. All cells showed the same feature changes.

Figure 4.4.2. shows a typical spectrum from within the nucleus after treatment with actinomycin D in comparison with a spectrum from within the cytoplasm and a spectrum of the pure compound. The spectra from within the cytoplasm do not show signs of drug accumulation or any other deviations from typical spectra of the cytoplasm. The spectra appear to be not just a superposition of a cell spectrum and the spectrum of actinomycin D, but differ drastically with respect to the original spectra. The C – C=N and C – C=C asymmetric stretches of the phenoxazone moiety at $1502cm^{-1}$ and $1481cm^{-1}$ loose much of their intensity and are now found at $1506cm^{-1}$ and $1487cm^{-1}$. Instead the intensities at $1456cm^{-1}$ and $1436cm^{-1}$ increase and become the predominant peaks in the spectra. Also very pronounced now the peak at $1575cm^{-1}$ which is found at the same position. The C – NH_2 bending at $1402cm^{-1}$ and the symmetric vibrations at $1263cm^{-1}$ and $1213cm^{-1}$ loose their intensity and disappear.

The spectral changes are quite dramatic and likely due to the intercalation of the phenoxazone fraction of the molecule into the DNA base pairs. That the spectra of actinomycin D are very sensitive to conformational changes has been noticed in the earlier studies in solution.[39] Changing the solvent from methanol to water has a great impact on the intensities of the spectra. Figure 4.4.3. shows a spectrum of acinomycin D in aqueous solution in comparison with the solid state spectrum and again a spectrum from within the nucleic region. The strongest intensity shows the peak at 1482cm^{-1} whereas the one at 1502cm^{-1} drastically drops. The peak at 1453cm^{-1} is still well pronounced but not as strong as in the spectrum from the nucleus. The origin of the peak has been assigned to an in plane vertical deformation of the phenyl fragment of the chromofore.[40] If one subtracts the underlying C – H bending intensity of the proteins the peak is still the most dominating feature of the spectrum.

In addition to the spectra of actinomycin D in solution the impact of DNA as well as oligo- and mononucleotides has been reported.[39] The authors find very little influence of the presence of nucleotides on the spectra in aqueous solution. The spectra do not significantly deviate from pure solution spectra. The apparent differences of the spectra from within the nucleus may indicate that the solution structures do not reflect the structures inside the chromatin.

The images b1-b5 show the intensities of the skeletal vibrations of the phenoxazone moiety between 1400cm^{-1} and 1500cm^{-1} in contrast to the amide I intensities. The spectral region is overlaid by the C – H bending modes of the proteins but appeared to be clearly enhanced. The intensity images superimposed on the microscopic pictures show the distribution of actinomycin D inside the cells. Based on the distribution

images one can see that the compound accumulates exclusively inside the nucleus, which is in contrast to the distribution found for the Hoechst compounds.

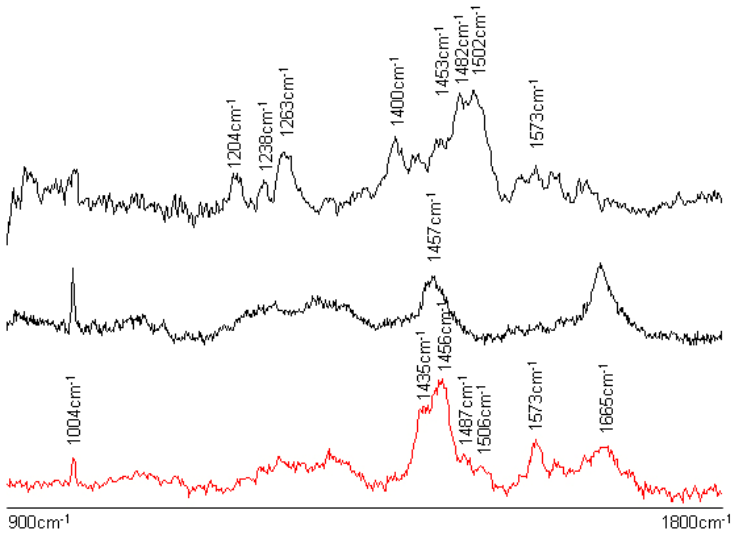

Figure 4.4.2.: Raman spectra from the nucleic region after treatment with actinomycin D (bottom) in comparison with a spectrum from the cytoplasm (middle) and a spectrum of actinomycin D (top)

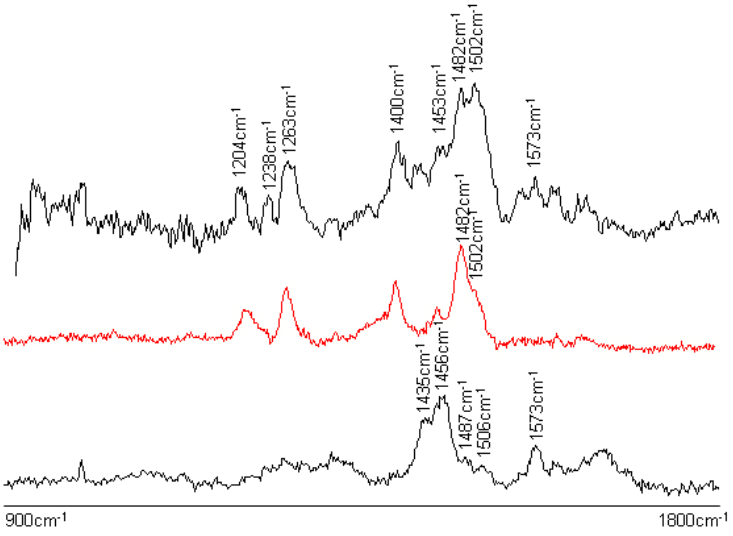

Figure 4.4.3.: Raman spectrum of actinomycin D in aqueous solution (middle) in comparison to a solid state spectrum (top) and a spectrum from within the nucleus of a cell after exposure (bottom)

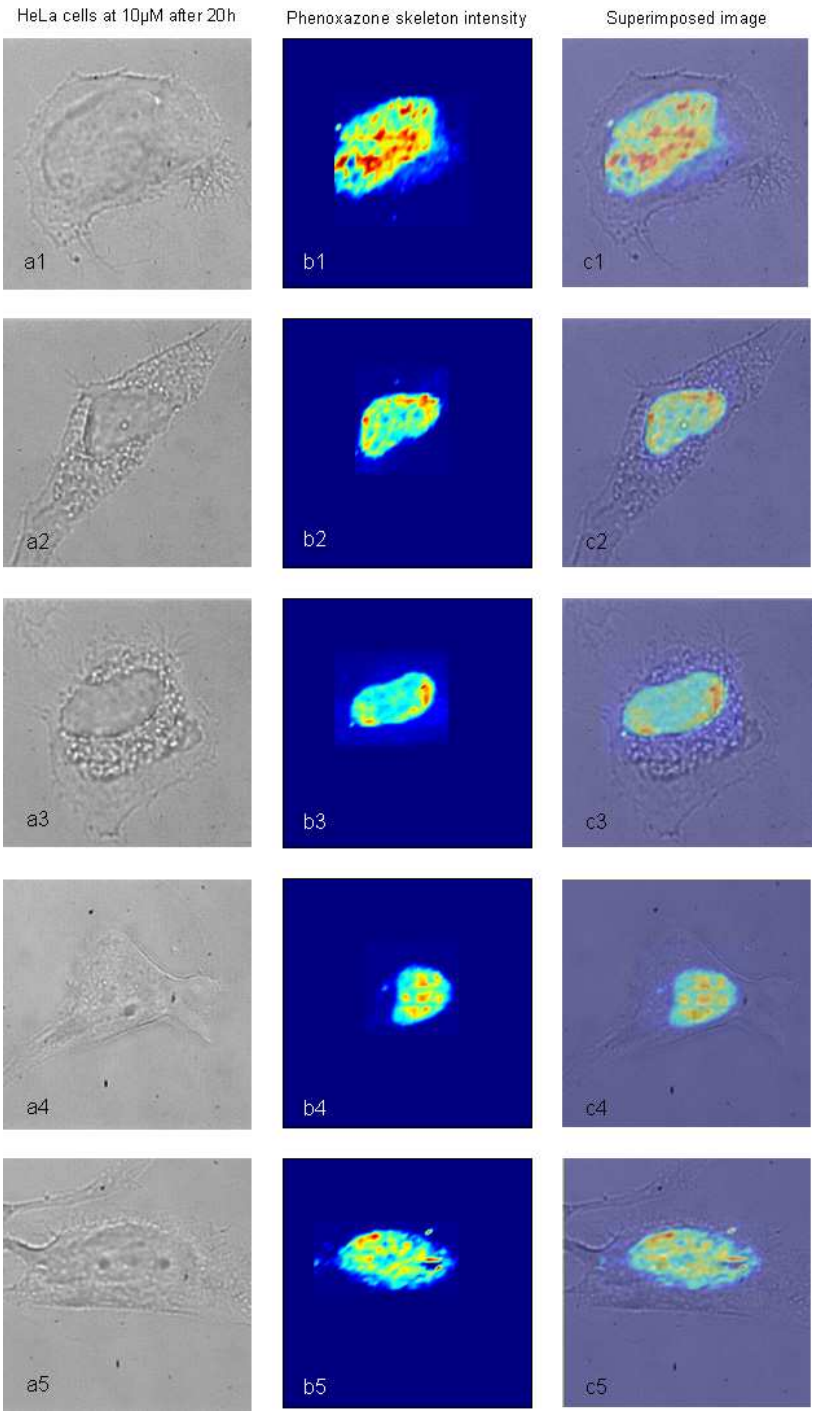

Figure 4.4.4.: Microscopic pictures of HeLa cells treated with actinomycin D at 10µM for 20h (a1-5). Images B1-3 are reconstructed from the phenoxazone skeleton vibrations between1400cm-1 and 1480cm-1. The overlaid images C1-3 show the distribution of actinomycin D inside the cells.

4.5. Acriflavine

Acriflavine (**7**) also intercalates into the DNA inhibiting replication. Its complexed structure with dCpG was first determined in 1980.[41] Although it has found its main applications for its anti-bacterial and anti-viral activity it has also been evaluated for potential tumor treatment *in vivo*.[42] Its structure is relatively simple and consists of an acridine core with two amino substitutions at the 3 and 6 positions and one methyl substation at the nitrogen. It is similar to that of the actinomycin D chromophore, but because of increased aromaticity more planar and less flexible.

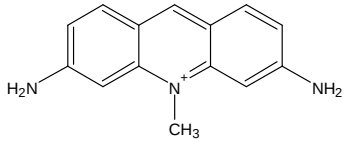

7

4.5.1. Results

The Raman spectrum of acriflavine in aqueous solution is shown in figure 4.5.1. A solid state spectrum could not be obtained because of strong fluorescence. Since the molecule is relatively rigid the solution spectrum should not differ from the solid state spectrum as much as in the case of actinomycin D. There are obvious similarities in comparison with the spectrum of actinomycin D. The band at 1636cm^{-1} shifts slightly to 1640cm^{-1} and appears at equal relative intensity. The acriflavine spectrum also shows a peak at 1570cm^{-1}. The most dominating features are between 1500cm^{-1} and 1300cm^{-1}. Again, there are three pronounced intensities between 1300cm^{-1} and 1100cm^{-1} located at 1231cm^{-1}, 1217cm^{-1} and 1180cm^{-1}. Spectra of close derivatives of acriflavine have been reported in the literature.[43] Structurally very similar are 9-aminoacridine and

quinacrine which has a secondary amino-substitution also at the 9 position. According to the assignments of the spectra of the two structures the following interpretation of the acriflavine spectrum is possible. The band at 1640cm^{-1} is likely due to a C – NH_2 in-plane bending, whereas the band at 1570cm^{-1} is due to the C – NH_2 stretching mode. The bands between 1500cm^{-1} and 1300cm^{-1} can be mainly attributed to the in-plane ring stretching vibrations. The spectra of 9-aminoacridine and quinacrine also show intensities between 1300cm^{-1} and 1100cm^{-1} similar to those in the spectra of acriflavine and actinomycin D. The authors interpret them as C – H in-plane bending contributions of the acridine, which differs from the assignments, made for the actinomycin D core. [43]

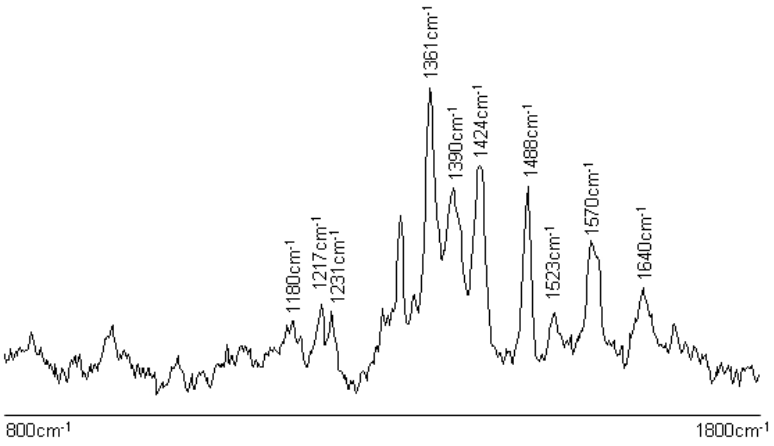

Figure 4.5.1.: Raman spectrum of 10mg/ml acriflavine in aqueous solution

Figure 4.5.3. a1-a5 show HeLa cells treated with 20µM of acriflavine for 30min. Apart from enlarged nucleoli the visible cellular features stay in shape. Most of the cells stayed adhered to the substrate. Longer exposure times or higher acriflavine concentrations resulted in further signs of degradation but resulted in high fluorescence disturbing the Raman signals.

Figure 4.5.2. shows a spectrum from within a cell treated with acriflavine compared to an untreated cell spectrum and the spectrum of acriflavine. All spectra from within the cell body differ from normal cell spectra. Again, the spectral changes are quite dramatic. The spectral region between 1400cm^{-1} and 1200cm^{-1} is most affected. The intensities at 1387cm^{-1} and 1228cm^{-1} obviously originate from the same intensities found in the spectrum of the pure compound. The new spectral feature between 1345cm^{-1} and 1280cm^{-1} is more difficult to interpret. It may originate from an increased intensity of the acriflavine peak at 1320cm^{-1}, which also appears to be at the same position. The small peaks at 1340cm^{-1} and 1298cm^{-1} also seem to reappear. The first is at the same position whereas the second is shifting to 1308cm^{-1} with an increase in intensity. The peaks at 1640cm^{-1} and 1424cm^{-1} probably merge with the peptide amide I and C – H bending bands respectively. The strong peaks at 1488cm^{-1} and 1361cm^{-1} disappear.

As mentioned above, all spectra from within the cell body differ from the normal cell spectra. The images b1-b5 in figure 4.5.3. show the intensities of the spectral region between 1345cm^{-1} and 1280cm^{-1} which reflect the distribution of acriflavine in the cell shown in the overlaid images c1-c5. Although the compound binds to DNA it does not exclusively accumulate in the nucleus. Furthermore, the spectra deviate only little among each other. Spectra from within the nuclei, nucleoli and cytoplasm are very similar. In other words, the spectral changes do not arise from the interaction with DNA. One possible explanation is that far more acriflavine molecules penetrate the nucleus than actually end up binding to DNA and that the spectral changes rather reflect interactions with proteins.

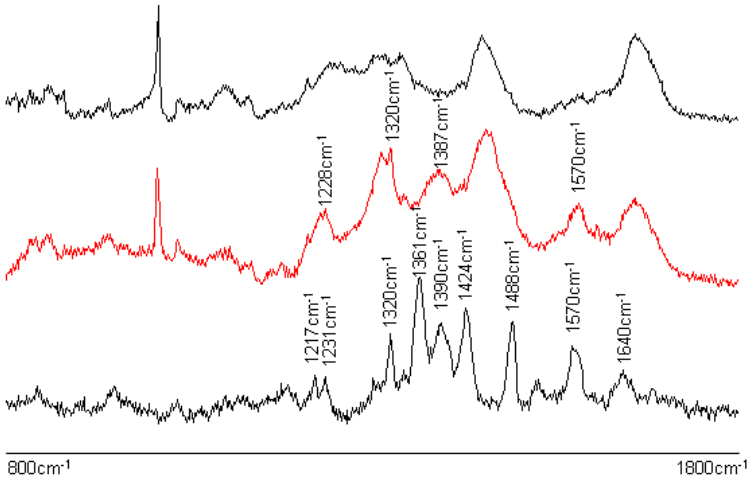

Figure 4.5.2.: Raman spectrum of a cell treated with acriflavine (middle) in comparison with a normal cell spectrum of an untreated cell (top) and a spectrum of acriflavine (bottom)

The experiments with amsacrine, camptothecin as well as the benzopyrene derivatives did not give any positive results.

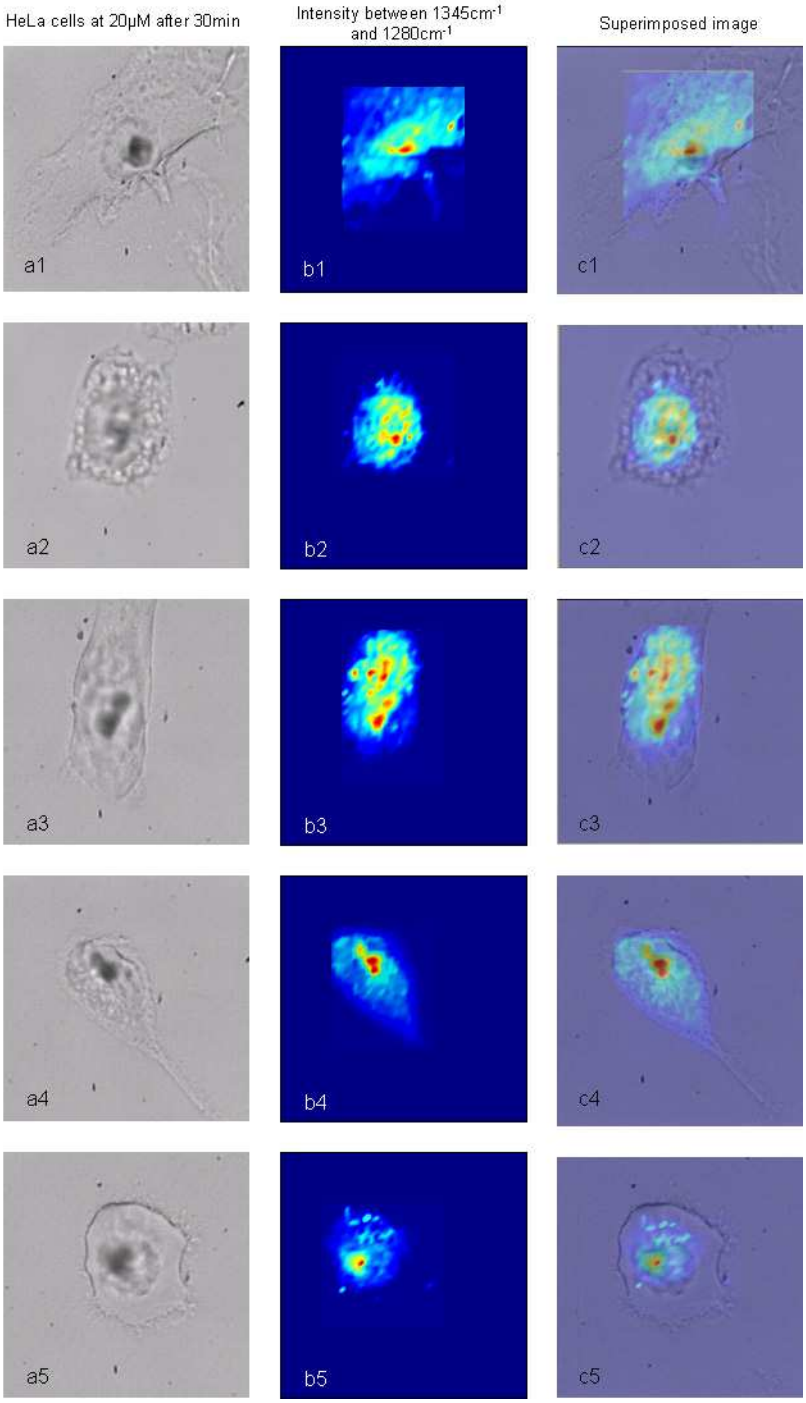

Figure 4.5.3.: Microscopic pictures of HeLa cells treated with acriflavine at 20µM for 30min (a1-a5). Images b1-b5 are reconstructed from intensities between 1345cm^{-1} and 1280cm^{-1}. The overlaid images c1-c5 show the distribution of acriflavine inside the cells.

4.6. Cyanoguanidines

The cyanoguanidines that have anti tumor properties belong to a group of guanidine-pyrimidines of which m-iodobenzylguanidine (MIBG) seems to be the most prominent. Lowering of the pH of cell culture medium and tumor tissue upon inoculation suggests that MIBG disturbs the mitochondrial respiratory system.[44] Employing electron spectroscopic imaging it was possible to show that MIBG accumulates exclusively in mitochondria.[45] Mitochondria inhibition is not a common feature among anticancer drugs and thus potentially interesting against multi drug resistance. Cells treated with cyano-derivatives of pyridyl-guanidines show similar reactions in terms of progressive acidification of cell culture medium. Among several derivatives a reagent bearing the code CHS 828 (**8**) turned out to be the most effective.[46]

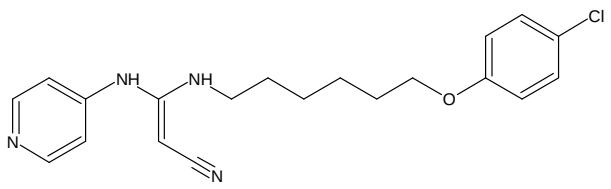

8

Apart from mitochondrial inhibition, CHS 828 shows interesting activity patterns that differ from well established cancer drugs. CHS 828 induces cell death features such as chromatin condensation, nuclear fragmentation and membrane blebbing that are typical for apoptosis. It was also possible to show p53 activation, a key event in triggering apoptosis.[47] On the other hand the process of cell death was found to be unaffected by caspase-3 inhibition. With the caspase cascade playing a central role in apoptosis, the activity mode of the drug can not be described as simply apoptotic.[48]

4.6.1. Results

The Raman spectrum of CHS 828 is shown in figure 4.6.1. The cyano-band located at 2188cm^{-1} is clearly one of the most prominent features of the spectrum. Also well pronounced is the C=C stretching of the guanidine moiety at 1601cm^{-1}. The ν_1 a_{1g} ring breathing of the chlorophenyl and pyridyl group apparently fall into the same position at 996cm^{-1}. The band at 819cm^{-1}could also originate from the chorophenyl fragment since ring vibrations of para-substituted benzenes appear within that range.

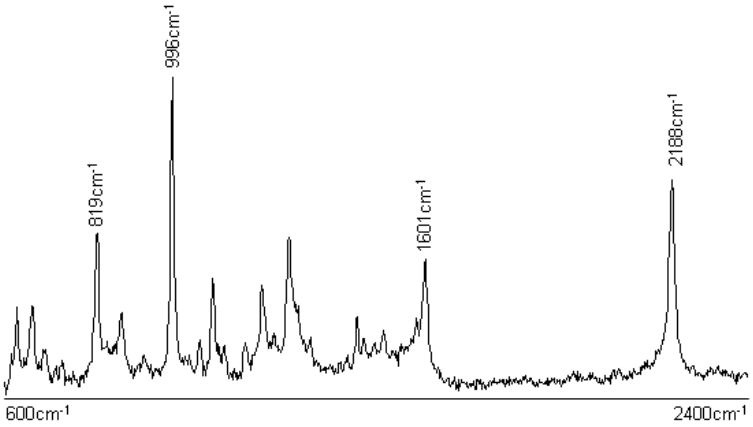

Figure 4.6.1.: Raman spectrum of CHS 828

Figure 4.6.3. a1-a5 are microscopic pictures of lymphoma cells treated with CHS 828 at a concentration of 500µM for one hour. All cells show deformation of the cell membranes indicating an advanced stage of cell degradation.

Figure 4.6.2. shows a spectrum from within the cell in comparison with a spectrum of CHS 828. The cyano-stretching mode is clearly pronounced and has shifted from 2188cm^{-1} to 2178cm^{-1}. No other bands of the compound contribute to the spectra of the treated cells. The resulting spectra are not a superposition of the spectral features of

the cells and the compound itself. The C=C stretching of the guanidine-fragment is not pronounced in the resulting spectra. The a_{1g} phenyl breathing merges, if it is present, with the a_{1g} phenylalanine peak. The shift of the cyano-band of about $10cm^{-1}$ is significant and may be due to a change of the structural arrangement in the cellular environment. It is also possible that the compound metabolizes upon uptake. The shift further into the red would involve a more extended delocalization of the triple bond into the guanidine-fragment. That is possible if one of the amino-linkages is affected.

Figure 4.6.3. b1-b5 are images reconstructed from the intensity of the Raman band of the cyano-stretching and c1-c5 reflect the distribution of the compound inside the cells. The distribution is not homogeneous and there are areas where the compound can not be detected. Figure .4.6.4. shows the spectra representing the intensity variation with respect to areas of high and low concentration.

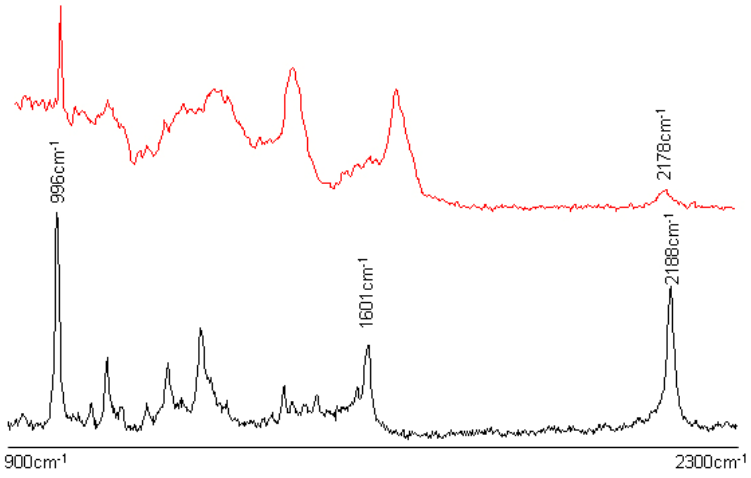

Figure 4.6.2.: Raman spectrum of a cell treated with CHS 828 (top) in comparison with a spectrum of the pure compound (bottom).

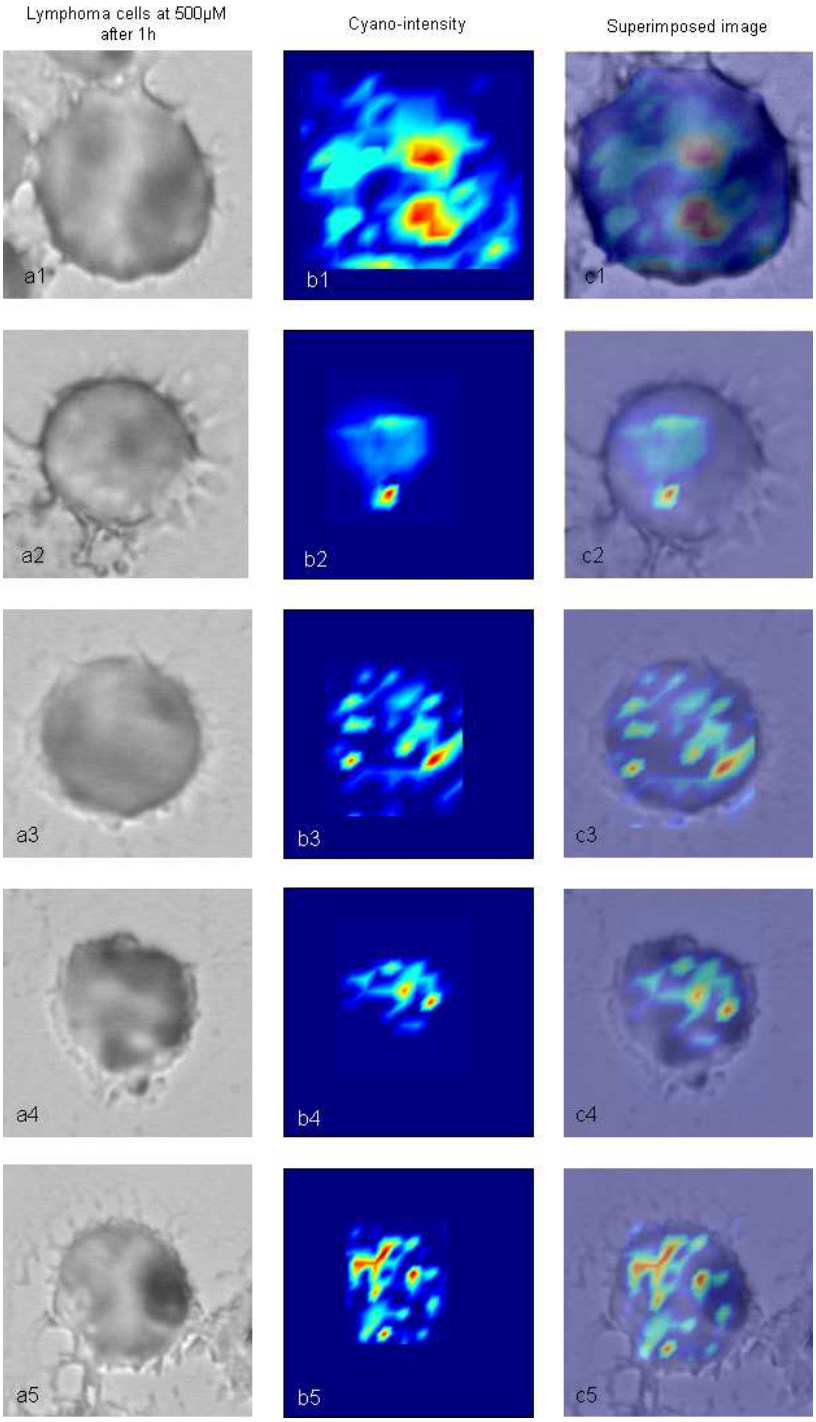

Figure 4.6.3.: Microscopic pictures of lymphoma cells treated with CHS 828 at 500µM for 1h (a1-a5). Images b1-b5 are reconstructed from the CN stretching vibration at 2178cm^{-1} which reflects the distribution of the compound inside the cells.

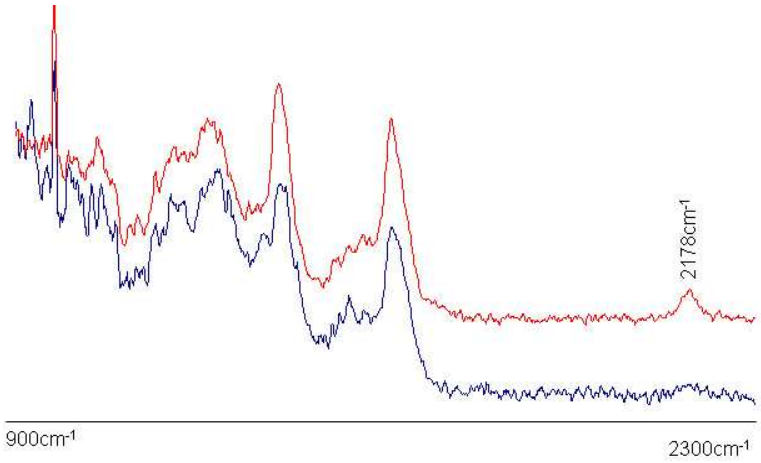

Figure 4.6.4.: Raman spectra corresponding to high and low cyano-intensity inside lymphoma cells.

4.6.2. Chemistry

One possible pathway to synthesize cyano-guanidines starts with dimethyl-N-cyanodithio-iminocarbonate (**9**) as key intermediate. Under basic conditions **9** undergoes an S_{N2} type coupling with primary amines. The reaction with 4-pyrimidinyl-analine (**10**) is selective at the stereochemically favored position. The remaining thioether is deactivated and thus (2Z)-3-(methylthio)-3-(pyridin-4ylamino)acrylonitril (**11**) the main product. The final compound is then readily obtained by a second coupling reaction with 6-(4-chlorophenoxy)hexan-1-amine (**12**).

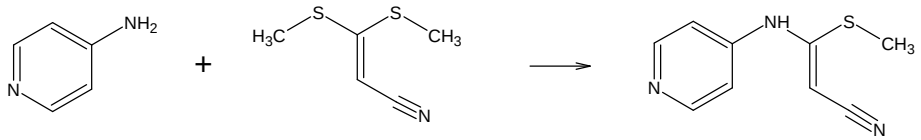

10 **9** **11**

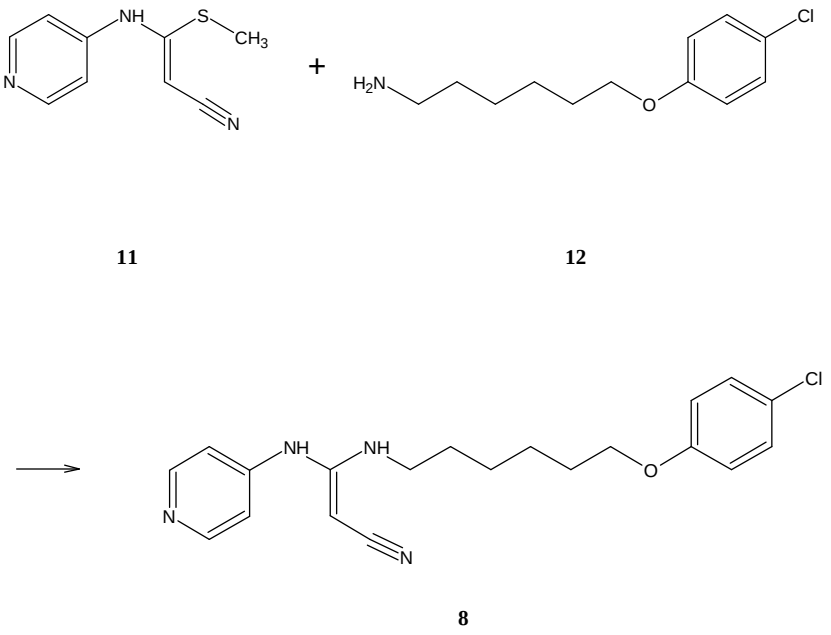

Scheme 3: Synthetic pathway for CHS 828

(2Z)-3-(methylthio)-3-(pyridin-4ylamino)acrylonitril: 5g (10mMol) of NaH (in 50% oil suspension) were slowly added to an ice-cold solution of 18g (123.43mMol) of the dithioether in DMF. After adding 10g of the 4-aminopyridin in 30ml DMF, the reaction mixture was cooled for six hours and stirred over night at room temperature. The product was precipitated with 50ml ether and 150ml ice cooled water. After filtration, the aqueous phase was treated with glacial acidic acid and filtrated. The precipitate was washed twice with acetone/ether (1:5) and finally rinsed with ether. The yield was 8.36g or 43.5%.

^{1}H-NMR(400MHz) ($CDCl_3$) : δ = 8.35 (d, 2H), 7.39 (d, 2H), 2.58 (s, 3H)

6-(4-chlorophenoxy)hexan-1-nitril: The nitrile was prepared according to a standard Williamson-ether-coupling reaction[49].

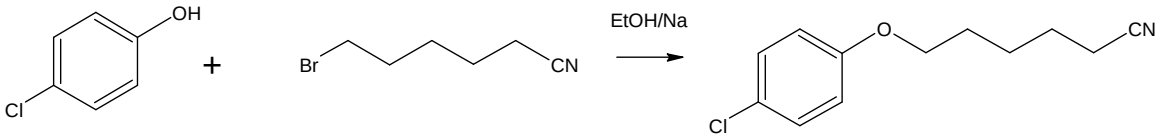

7.71g (60mMol) of the 4-chloro-phenol were dissolved in 25ml ethanol and added to a solution of 0.29g (12.5mMol) of sodium in 100ml anhydrous ethanol. The bromo-hexanitrile was also dissolved in 25ml of ethanol on added drop wise under argon. After the reaction mixture was refluxed for six hours, ethanol was separated by distillation. 35ml ether were added to the mixture and washed with 30ml 2M NaOH for three times. The aqueous phase was again treated with 30ml of ether and tried over $CaCl_2$. After distilling the ether 1.59g (7.11mMol) or 71.1% product were recovered.

^{1}H-NMR (400MHz) ($CDCl_3$): δ = 7.25 (d, 2H), 6.80 (d, 2H), 3.95 (t, 2H), 2.41 (t, 2H), 1.50-2.00 (m, 8H)

6-(4-chlorophenoxy)hexan-1-amine: To 150ml anhydrous ethanol 0.4g (10.66mMol) of $LiAlH_4$ were added at 0˚C. 1.59g (7.11mMol) in 50ml ethanol were slowly added and stirred under argon over night. Any remaining hydride was reduced by 10ml ethylacetate in 20ml ethanol. Roughly 7ml saturated Na_2SO_4 were added to precipitate $Al(OH)_3 \times H_2O$ from the emulsion. The white precipitate was filtrated the solution dried with Na_2SO_4 and the ether evaporated. After ten hours drying under vacuum 1.361g were recovered, which is equivalent to a yield of 84.1%.

^{1}H-NMR (400MHz) ($CDCl_3$): δ = 7.20 (d, 2H), 6.82 (d, 2H), 3.90 (t, 2H), 2,70 (t, 2H)1.70-2.20 (m, 8H), 1.7-1.1 (m, 2H, NH)

N-(6-(4-chlorophenoxy)hexyl-N'-cyano-N"-4-pyridylguanidine: 1.36g (5.98mMol) of the thioether and 1.15g of triethylamine were dissolved in 45ml pyridine. The amine was added drop wise with 20ml pyridine. The reaction mixture was heated under argon at 55-70˚C for seven hours and stirred over night. Pyridine was distilled and the remaining 5-10ml were treated with 30ml ice cooled ether. The precipitate was filtered and washed with ether for three times.

^{1}H-NMR (400MHz) (DMSO-d_6): δ = 8.31 (d, 2H), 7.29 (d, 2H), 7.20 (m, 2H), 6.91 (m, 2H), 3.95 (t, 2H), 3.22 (m, 2H), 1.71 (m, 2H), 1.58 (m, 2H), 1.4 (br, 2H, NH)

4.7. Cyanoaziridines

The cyanoaziridines described in the literature derive from a substance called imexon (**13**) which showed potential activity in a variety of animal studies and is now in clinical trials phase I. In water, imexon undergoes a slow conversion into 2-cyanoaziridine-1-carboxamide (**14**).

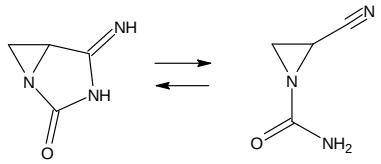

13 **14**

Since the chemistry of both compounds seems to be closely related a number of derivatives of the carboxamide have been tested in vitro. All of which had reasonable IC_{50} values.[50] Imexon is believed to act in a number of ways that are likely related to

an opening of the aziridine ring. Aziridine rings are common components in a number of cytotoxins such as mustard agents or mitomycin C. Usually those structures bind to cellular and nuclear DNA by alkylation of the purin and pyrimidine bases. However, no DNA alkylation was found after lethal incubation with Imexon. Instead, aqueous solution studies show alkylation of sulfurhydryl groups of cystein residues and glutathione an important non-enzymatic antioxidant. Depletion of glutathione could be demonstrated as well as reactive oxygen species increase which leads to oxidative damage of cellular DNA.[51] Furthermore, Imexon causes swelling of mitochondria resulting in cytochrome C release into the cytoplasm, triggering apoptosis.[52, 53]

4.7.1. Results

Figure 4.7.1. shows the Raman spectra of imexon as well as the two synthesized derivatives. The imexon spectrum is dominated by two out of plane ring vibrations at 651cm^{-1} and 682cm^{-1} which are surprisingly strong. The C=O and C=N as well as the amide vibrations lie between 1665cm^{-1} and 1755cm^{-1} and the cyclopropane and cyclopentane ring breathing modes are at 1188cm^{-1} and 866cm^{-1} respectively. The spectrum of 2-cyanoaziridine-1-(N-(ethyl-))carboxamide has a very strong cyano-band at 2253cm^{-1}. The carbonyl-band is at 1660cm^{-1} far less pronounced and the cyclopropane ring breathing at 1146cm^{-1}. The strongest peak of the phenyl derivative is the a_{1g} ring vibration at 997cm^{-1}. The cyano-stretching is unfortunately far less pronounced at 2251cm^{-1}. The carbonyl stretch is at 1670cm^{-1} and the amide stretch at 1598cm^{-1}.

Figure 4.7.3. a1-a5 shows lymphoma cells treated with 10mM 2-cyanoaziridine-1-(N-(ethyl-))carboxamide for 2h. The cells do not show any apparent features of degradation but further treatment eventually led to cell death.

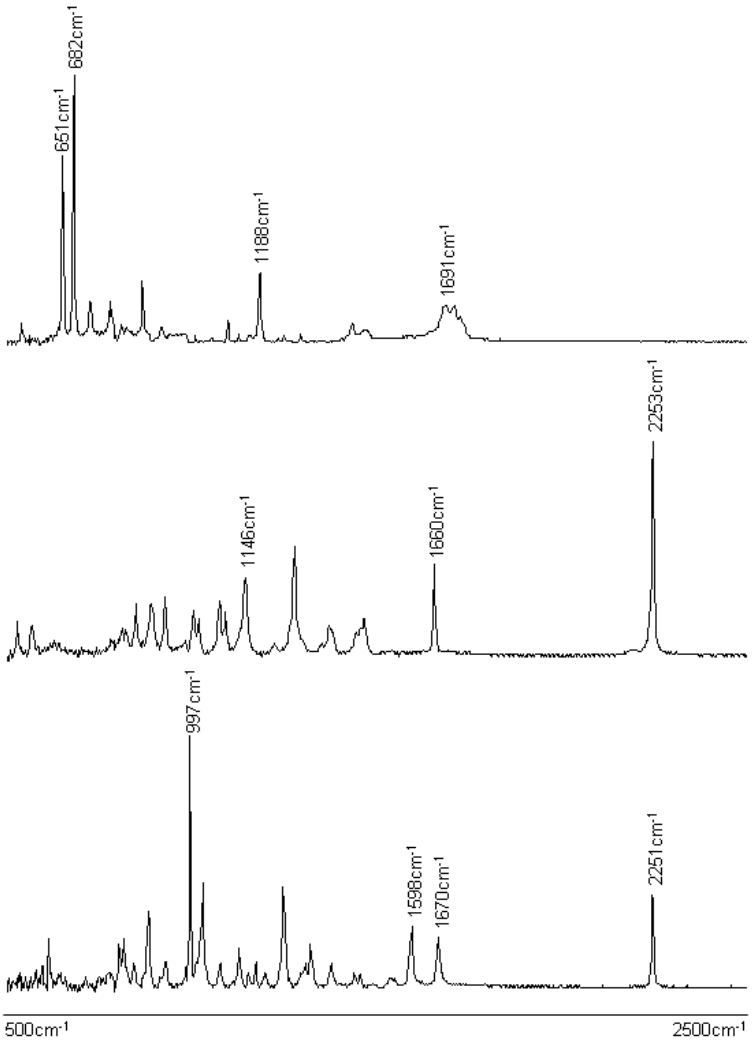

Figure 4.7.1.: Raman spectra of imexon (top), 2-cyanoaziridine-1-(N-(ethyl-))carboxamide (middle) and 2-cyanoaziridine-1-(N-(phenyl-)carboxamide (bottom)

Figure 4.7.2. shows a spectrum of a cell treated with 2-cyanoaziridine-1-(N-(ethyl-))carboxamide. The cyano-band appears at 2253cm^{-1} and has, in contrast to the cyano-guanidine experiment, not shifted indicating that the compound is not metabolized. Again, no other bands of the cyano-drug contribute to the spectrum. Interestingly, the spectra of the cell itself have a different appearance. The additional peak at 1753cm^{-1} is usually associated with ester carbonyl-stretches of phospholipids. Normally they construct the membrane of smaller vesicles, which are too thin or too small to be detected. However, due to metabolic changes it is possible that phospholipids are produced by the cell and thus accumulate to a great extend.

The distribution of the cyano-compound is shown id figure 4.7.3. b1-b5 and c1-c5. Again, the distribution is not homogeneous and there are regions where it can not be detected.

The experiments with Imexon did not show positive results. Neither the cyano-region had any additional peaks, which could have been possible due to the conversion mentioned in the introduction. Nor did the two strong peaks from the ring deformation contribute to the spectra. The experiments with the phenyl derivative also gave negative results.

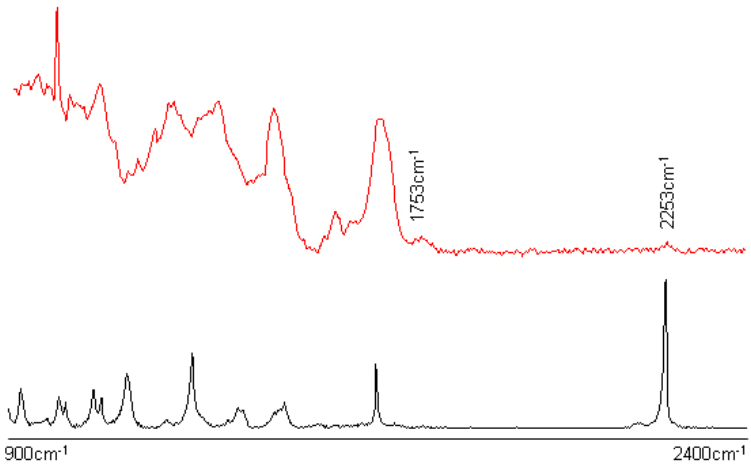

Figure 4.7.2.: Raman spectrum of a cell treated with 2-cyanoaziridine-1-(N-(ethyl-))carboxamide (top) and Raman spectrum of the compound (bottom).

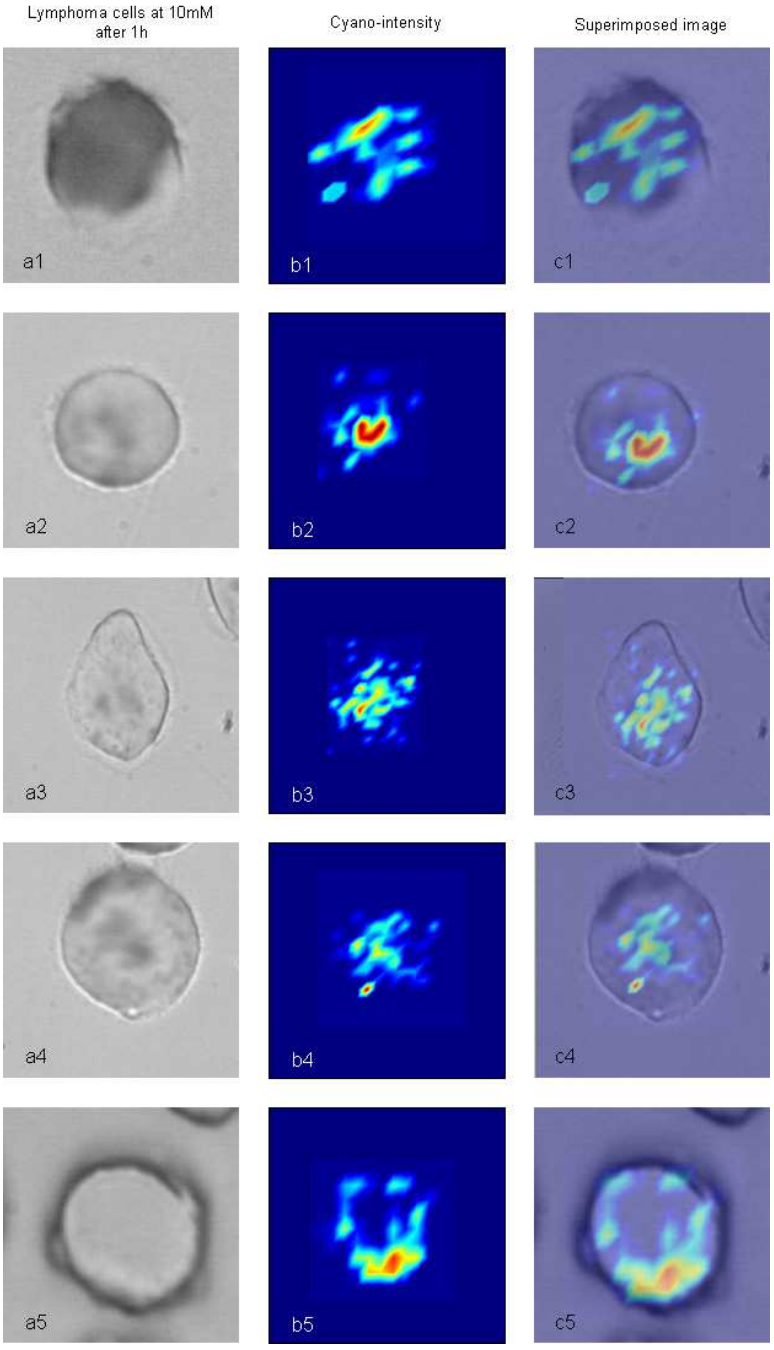

Figure 4.7.3.: Microscopic pictures of lymphoma cells treated with 10mM of 2-cyanoaziridine-1-(N-(ethyl-))carboxamide for 1h (a1-a5). Images b1-b5 are reconstructed from the CN stretching vibration at 2178cm^{-1} which reflects the distribution of the compound inside the cells. C1-5 Are the superimposed presentations of a1-5 and b1-5

4.7.2. Chemistry

Aziridine-carboxamides can be synthesized by a relatively simple addition reaction of the aziridine and an appropriate isocyanate (scheme 4.1.). The cyano-aziridines are accessible via a successive substitution of 2,3 dibromo-propanenitril (scheme 4.2.). The desired isocyanates are commercially available.

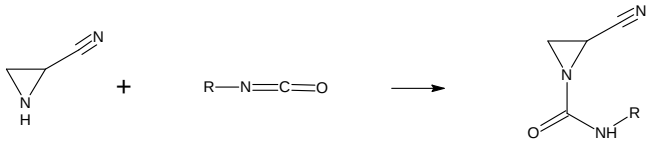

Scheme 4.1.: Synthesis of cyanoaziridine-carboxamides

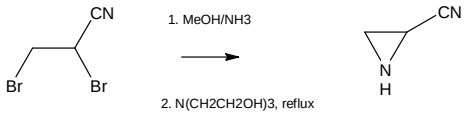

Scheme 4.2.: Synthesis of cyanoaziridine

2-Cyanoaziridine: To 80ml of ice-cooled methanol, saturated with gaseous ammonia 25g (0.117mol) of the 2,3 dibromo-propanenitril were slowly added. After 1h 35g of triethanolamine were dissolved and the mixture refluxed for 4h. The triethanolhydrobromide was filtered, washed with methanol and the solvent distilled under vacuum. The solution was mixed with 7ml 2N H_2SO_4 and adjusted to pH 6 with $NaHSO_4$. After extraction with ethylacetate the product was chromatographically purified over Al_2O_3. 2.94g (37%) of the aziridine were recovered.

^{1}H-NMR (400MHz) ($CDCl_3$): δ = 2.53-2.63 (m, 1H, CH), 2.15-2.25 (m, 2H, CH_2), 1.05 (br s, 1H, NH)

2-cyanoaziridine-1-(N-(ethyl-))carboxamide: To 1g (0.015mol) of the aziridine in 20ml ice-cooled toluene1.42g (0.02mol, 1.57ml) of ethylisocyanate were added. The mixture was stirred for 5h and refrigerated over night. The precipitate was filtered and washed with toluene. 2.08g (99%) were recovered.

^{1}H-NMR (400MHz) ($CDCl_3$): δ = 6.15 (br s, 1, NH), 3.19 (q, 2H,), 2.97 (dd, 1H), 2.50 (d, 1H), 2.40 (d, 2H), 1.10 (t, 3H)

2-cyanoaziridine-1-(N-(phenyl-))carboxamide: As above yielding 91%.

^{1}H-NMR (400MHz) (DMSO-d_6): δ = 10.20 (br s, 1H, NH), 7.40 (d, 2H), 7.30 (d, 2H), 7.12 (t, 1H), 3.12 (dd, 1H), 2.68 (d, 1H), 2.55 (d, 1H)

4.8. Discussion

For the groove binding bisbenzimidazoles as well as for two intercalating systems it was possible to show that Raman microscopy is a feasible technique to study drug distribution inside cells. The conventional Raman scattering from the active agents is apparently strong enough to perturb the signals from their cellular environment. In the case of the Hoechst agent, the spectra of the treated cells appear to be a superposition of the spectra of the compound itself and the spectra from the cell. The interaction between the compound and the DNA or any other cellular material has virtually no effect on the spectra. For the intercalating systems the spectral appearance changes drastically and the resulting spectra can not be seen as a superposition of the drugs and the cellular components. The intensities and positions of the individual peaks are affected. Some peaks completely disappear. Interestingly the spectral changes associated with the uptake do not seem to be caused by the interaction with DNA. For Actinomycin D the Raman studies in solution do not reflect the spectral changes observed inside the cells. For Acriflavine the spectra from within the nucleus and from the cytoplasm are too similar. Given that most of the nucleus consists of proteins the results may not be too surprising. It is by all means possible that more of the compound accumulates than actually binds to DNA. So that changes due to the interactions with DNA are not detected. Two different distributions were found. The Hoechst compounds and Acriflavine are distributed through the whole cell body whereas Actinomycin D is exclusively detected in the nuclei.

With respect to the concentration inside the cells one can say that it is far greater than in the surrounding medium. The detection limit for those compounds was roughly

500µM. At the applied concentrations of 10µM to 50µM no Raman signal could be obtained from the medium.

Apart from the three cases with astonishing results there are a variety of experiments with compounds that could not be detected. The symmetric bisbenzimidazole and Distamycin as groove binding systems as well as Amsacrine, Camptothecin and the benzopyrenes as intercalators did not yield suffitient signal inside the cells. The negative results are especially surprising in the case of the symmetric bisbenzimidazole and Amsacrine since both structures are very similar to those that gave positive results. There are two reasonable explanations. For one it is possible that not enough of the substances accumulate inside the cells so that the concentration is too low to be detected. The other possibility is that the compounds that could be detected have unique electronic properties, which allow resonance effects. The detectability in the submillimolar range certainly supports that argument. All other compounds did not give enough signal at concentrations lower than 10mM.

The imaging experiments were also successful for two of the cyano drugs. The observed shift of the cyano peak position of the guanidine compound can possibly be explained by metabolic activity after the uptake. The peak position of the cyano-aziridine did not move indicating that its structure does not change. In both cases the distribution of the compounds in the cell was not even. The experiments also show the limits of conventional Raman microscopy. It is only possible to detect vibrations, which are extremely isolated. All other peaks of the compounds blend into the spectra of the cells components due to the coupling of the vibrational modes. Very problematic are the applied concentrations which lie roughly hundredfold above the critical concentrations.

From the pharmaceutical point of view, this is hardly acceptable. At this overdose the mode of action which determines the faith of the cells may be different than for lower exposure concentrations and the distributions may not reflect certain affinities of the compounds for certain cellular compartments.

Chapter 5: References

1. **Sijtsema, N.M., Tibbe, A. G., Segers-Nolten, I. G., Verhoeven, A. J., Weening, R. S., Greve, J., Otto, C., *Intracellular reactions in single human granulocytes upon phorbol myristate acetate activation using confocal Raman microscopy.* Biophysical Journal, 2000. 78(5): p. 2606-13.**

2. **Otto, C., Sijtsema, N. M., Greeve, J., *Confocal Raman microspectroscopy of the activation of single neutrophilic granulocytes.* European Biophysical Journal, 1998. 27(6): p. 582-589.**

3. **Sijtsema, N.M., Otto, C., Segers-Nolten, I. G., Verhoeven, A. J., *Resonance Raman microspectroscopy of myeloperoxidase and cytochrome b558 in human ganulocytes.* Biophysical Journal, 1998. 74(6): p. 3250-3255.**

4. **van Manen, H.J., Kraan, Y. M., Roos, D., Otto, C., *Single-cell Raman adn fluorescence microscopy reveal the association of lipid bodies with phagosomes in leucocytes.* Proceedings of the National Academy of Science USA, 2005. 102(29): p. 10159-10164.**

5. **Wood, B.R., Hammer, L., McNaughton, D., *Raman microspectroscopy and imaging provides insights into heme aggregation and denaturation within human erythrocytes.* Journal of Biomedical Optics, 2005. 10(1): p. 14005.**

6. **Verrier, S., Notinger, I., Polak, J. M., Hench, L. L., *In situ monitoring of cell death using Raman microspectroscopy.* Biopolymers, 2004. 74(1-2): p. 157-162.**

7. **Nithipatikom, K., McCoy, M. J., Hawi, S. R., Nakamoto, K., Adar, F., Campbell, W. B., *Characterization and application of Raman labels for confocal Raman microspectroscopic detection of cellular proteins id single cells.* Analytical Biochemistry, 2003. 322(2): p. 198-207.**

8. **Uzunbajakava, N., Lenferic, A., Kraan, Y., Volokhina, E., Vrensen, G., greve, J., Otto, C., *Nonresonant confocal Raman imaging of DNA and protein distribution in apoptotic cells.* Biophysical Journal, 2003. 84(6): p. 3968-3981.**

9. **Huang, Y.S., Karashima, T., Yamamoto, M., Hamaguchi, H. O., *Molecular-level investigation of the structure, transformation, and bioactivity of single***

living fission yeast cells by time- amd space-resolved Raman spectroscopy. **Biochemistry, 2005. 44(30): p. 10009-10019.**

10. **Feofanov, A.V., Grichine, A. I., Shitova, L. A., Karmakova, T. A., Yakubovskaya, R. I., Egret-Charlier, M., Vigny, P., *Confocal Raman microspectroscopy and imaging study of theraphthal in living cancer cells.* Biophysical Journal, 2000. 78(1): p. 499-512.**

11. **Uzunbajakava, N., Otto, C., *Combined Raman and contineous-wave-excited two-photon fluorescence cell imaging.* Optics Letters, 2003. 28(21): p. 2073-2075.**

12. **Koljenovic, S., Schut, T. B., Vincent, A., Kros, J. M., Puppels, G. J., *Detection of meningioma in dura matter by Raman spectroscopy.* Analytical Chemistry, 2005. 77(24): p. 7958-7965.**

13. **Krishna, C.M., Sockalingum, G. D., Venteo, L., Bhat, R. A., Kushtagi, P., Pluot, M., Manfait, M., *Evaluation of the suitability of ex vivo handled ovarian tissues for optical diagnosis by Raman microspectroscopy.* Biopolymers, 2005. 79(5): p. 269-276.**

14. **Krishna, C.M., Sockalingum, G. D., Kurien, J., Venteo, L., Pluot, M., Manfait, M., Kartha, V. B., *Micro-Raman spectroscopy for optical pathology of oral squamous cell carcinoma.* Applied Spectroscopy, 2004. 58(9): p. 1128-1135.**

15. **Kirschner, C., Maquelin, K., Pina, P., Ngo Thi, N. A., Choo-Smith, L. P., Sockalingum, G. D., Sandt, C., Ami, D., Orsini, F., Doglia, S. M., Allouch, P., Mainfait, M., Puppels, G. J., Naumann, D., *Classification and identification of enterococci: a comparitive phenotypic, genotypic, and vibrational spectroscopic study.* Journal of Clinical Microbiology, 2001. 39(5): p. 1763-1770.**

16. **Huang, W.E., Griffiths, R. I., Thompson, I. P., Bailey, M. J., Whiteley, A. S., *Raman microscopic analysis of single microbial cells.* Analytical Chemistry, 2004. 126(41): p. 13226-13227.**

17. **Schuster, K.C., Reese, I., Urlaub, E., gapes, J. R., Lendl, B., *Multidimensional information on the chemical composition of single bacterial cells by confocal Raman microspectroscopy.* Analytical Chemistry, 2000. 72(22): p. 5529-5534.**

18. Weidlein, J., Mueller, U., Dehnicke, K., *Schwingungsspectroscopie*. 1982, Stuttgart, New York: Georg Thieme Verlag.

19. Schwabe, K., *Physikalische Chemie*. 1986, Berlin: Akademie Verlag.

20. Juang, C.B., Finzi, L., Bustamante, C. J., Revies of Scientific Instruments, 1988. 59: p. 2399.

21. Everall, N., *Depth profiling with concocal Raman microscopy, part 1.* Spectroscopy, 2004. 19(10): p. 22-27.

22. Ingle, J.D., Crouch, S. T., *Spectrochemical Analysis*. 1988: Prentice-Hall, Inc.

23. Savitzky, A., Golay, M. J. E., *Smoothing and differentiation of data by simplified least squares procedures.* Analytical Chemistry, 1964. 36(8): p. 1627-1639.

24. Steller, W., Einenkel, J., Horn. L.C., Braumann, U.D., Binder, H., Salzer, R., Krafft, C., *Delimitation of squamous cell cervical carcinoma using infrared microspectroscopic imaging.* Analytical and Bioanalytical Chemistry, 2006. 384(1): p. 145-154.

25. Wood, B.R., Chiriboga, L., Yee, H., Quinn, M. A., McNaughton, D., Diem, M., *Fourier transform infrared (FTIR) spectral mapping of the cervical transformation zone, and displastic squamous epithelium.* Cynecologic Oncology, 2004. 93: p. 59-68.

26. Spiro, T.G., *Biological Applications of Raman Spectroscopy*. Vol. 1. 1987: John Wiley & Sons, Inc.

27. Voet, D., Voet, J. G., *Biochemistry*. 1995, USA: John Wiley & Sons, Inc.

28. Chen, Y.-M., Huang, D.-H., Lin, S.-F., Lin, C.-Y., Key, J. L., *Fractionation of Nucleoli from Auxin-Treated Soybean Hypocotyl into Nucleolar Chromatin and Preribosomal Particles.* Plant Physiol., 1983. 73(3): p. 746-753.

29. **Pacifico, A., Chiriboga, L. A., Lasch, P., Diem, M.,** ***Infrared spectroscopy of cultured cells II. Spectra of exponentially growing, serum-deprived and confluent cells.*** **Vibrational Spectroscopy, 2003. 32: p. 107-115.**

30. **Diem, M., Chiriboga, L. A., Lasch, P., Pacifico, A.,** ***IR spectra and IR spectral maps of individual normal and cancerous cells.*** **Biopolymers (Biospectroscopy, 2002. 67: p. 349-353.**

31. **Monks, A., Scudiero, D. A., Johnson, G. S., Paull, K. D., Sausville, E. A.,** ***The NCI anti-cancer drug screen: a smart screen to identify effectors of novel targets.*** **Anti-Cancer Drug Design, 1997. 12: p. 533-541.**

32. **Uzunbajakava, N., Otto, C.,** ***Combined Raman and continuous-wave-excited two-photon fluorescence cell imaging.*** **Optics Letters, 2003. 28(21): p. 2073-2075.**

33. **Kraut, E.H., Fleming, T., Segal, M., Neidhart, J. A., Behrens, B. C., MacDonald, J.,** ***Phase II study of pibenzimol in pancreatic cancer.*** **Investigational New Drugs, 1991. 9: p. 95-96.**

34. **Bielawski, K., Bielawska, A., Wolcczynski, S.,** ***Synthesis, DNA-binding activity and cytotoxicity of carbamate derivatives of Hoechst 33258 in breast cancer MCF-7 cells.*** **Biol. Pharm. Bull., 2002. 25(7): p. 916-919.**

35. **Mann, J., Baron, A., Opoku-Boahen, Y., Johansson, E., Parkinson, G., Kellard, L. R., Neidle, S.,** ***A new class of symmetric bisbenzimidazole-based DNA minor groove-binding agents showing antitumor activity.*** **J. Med. Chem., 2001. 44: p. 138-144.**

36. **Neidle, S., Mann, J., Rayner, E. L., Baron, A., Opoku-Boahnen, Y., Simpson, I. J., Smith, N. J., Fox, K. R., Hartley, J. A., Kelland, L. R.,** ***Symmetric bis-benzimidazoles: new sequence-selective DNA-binding molecules.*** **Chem. Commun., 1999: p. 929-930.**

37. **Bailly, C., Chessari, G., Carrasco, C., Joubert, A., Mann, J., Wilson, W. D., Neidle, S.,** ***Sequence specific minor groove binding by bisbenzimidazoles: water molecules in ligand recognition.*** **Nucleic Acids Res., 2003. 31(5): p. 1514-1524.**

38. **Muller, W., Crother, D.M.,** ***Studies of binding of Actinomycin and related compounds.*** **Journal of Molecular Biology, 1968. 35: p. 251-290.**

39. **Chinsky, L., Turpin, P. Y., Duquesne M.,** ***Resonance Raman study of Actinomycin D interaction with DNA and its models.*** **Biochemical and Biophysical Research Communications, 1975. 65(4): p. 1440-1446.**

40. **Smulevich G., A.L., Marzocchi M. P.,** ***Raman excitation profiles of Actinomycin D.*** **Biochimica et Biophysica Acta, 1980. 610: p. 384-391.**

41. **Shieh H. S., B.H.M., Dabrow M., Neidle S.,** ***The structure of drug-deoxydinucleoside phosphate complex; generalized conformational behavior of intercalation complexes with RNA and DNA fragments.*** **Nucleic Acids Res., 1980. 8(1): p. 85-97.**

42. **Kim, S.G., Kim, C. W., Ahn, E. T., Lee, K. Y., Hong, E. K., Yoo, B. I., Han, Y. B.,** ***Enhanced anti-tumor effects af acriflavine in combination with guanosine in mice.*** **Journal of Pharmacy and Pharmacology, 1997. 49(2): p. 216-222.**

43. **Rivas, L., Murza, A., Sanchez-Cortes, S., Garcia-Ramos, J. V.,** ***Adsoption of acridine drugs on silver: surface-enhanced resonance Raman evidence of the existence of different adsorption sides.*** **Vibrational Sectroscopy, 2001. 25: p. 19-28.**

44. **Ekelund, S., Nygren, P., Larsson, R.,** ***Guanidino-containing drugs in cancer chemotherapy: biochemical and clinical pharmacology.*** **Biochemical Pharmacology, 2001. 61: p. 1183-1193.**

45. **Gaze, M.N., Huxam, I. M., Mairs, R. J., Barrett, A.,** ***Intracellular localization of metaiodobenzyl guanidine in human neuroblastoma cells by electron spectroscopic imaging.*** **International Journal of Cancer, 1991. 47: p. 875-880.**

46. **Vig Hjarnaa, P.J., Jonsson, E., Latini, S, Dhar, S., Larssom, R., Bramm, E., Skov, T., Binderup, L.,** ***CHS 828, a novel pyridyl cyanoguanidine with potent antitumor activity in vitro and in vivo.*** **Cancer Research, 1999. 59: p. 5751-5757.**

47. **Wojciechowski, J., Lovborg, H., Wesierska-Gadek, J.,** ***Activation of p53 protein in normal and in tumor cells by a novel anticancer agent CHS 828.*** **Drugs under experimental clinical research, 2003. 29(2): p. 53-67.**

48. **Martinsson, P., de la Torre, M., Binderup, L., Nygren, P., Larsson, R.,** ***Cell death with atypical features induced by the novel antitumoral drug CHS 828, in human U-937 GTB cells.*** **European Journal of Pharmacology, 2001. 417: p. 181-187.**

49. ***Organikum*****. 1975, Berlin: VEB Deutscher Verlag der Wissenschaften. 223.**

50. **Iyengar, B.S., Dorr, R. T., Alberts, D. S., Hersh, E. M., Salmon, S. E., Remers, W. A.,** ***Novel Antitumor 2-Cyanoaziridine-1-carboxamids.*** **Journal of Medicinal Chemistry, 1999. 42: p. 510-514.**

51. **Dvorakova, K., Payne, C. M., Tome, M. E., Briehl, M. M., McClure, T., Dorr, R. T.,** ***Induction of Oxidative Stress and Apoptosis in Myeloma Cells by the Aziridine Containing Agent Imexon.*** **Biochemical Pharmacology, 2000. 60: p. 749-758.**

52. **Dvorakova, K., Waltmire, C. N., Payne, C. M., Tome, M. E., Briehl, M. M., Dorr R. T.,** ***Induction of Mitochondrial Changes in Myeloma Cells by Imexon.*** **Blood, 2001. 97(11).**

53. **Evens, A.M., Prachand, S., Shi, B., Paniaqua, M., Gordon, L. I., Gartenhaus, R. B.,** ***Imexon Induced Apoptosis in Multiple Myeloma Tumor Cells Is Caspase-8 Dependent.*** **Clinical Cancer Research, 2004. 10: p. 1481-1491.**